

## Full length article

# Grain boundary properties of a nickel-based superalloy: Characterisation and modelling

E. Alabort <sup>a, b</sup>, D. Barba <sup>a, b</sup>, S. Sulzer <sup>b</sup>, M. Lißner <sup>a</sup>, N. Petrinic <sup>a</sup>, R.C. Reed <sup>a, b, \*</sup>

<sup>a</sup> Department of Engineering Science, University of Oxford, Parks Road, Oxford, OX1 3PJ, United Kingdom

<sup>b</sup> Department of Materials, University of Oxford, Parks Road, Oxford, OX1 3PH, United Kingdom

## ARTICLE INFO

## Article history:

Received 21 December 2017

Received in revised form

21 March 2018

Accepted 22 March 2018

Available online 2 April 2018

## Keywords:

Superalloys

Grain boundaries

Damage modelling

Crystal plasticity

Scanning electron microscopy

## ABSTRACT

Miniaturised tensile tests coupled with in-situ scanning electron microscopy are used to deduce the grain boundary properties of a nickel-based superalloy at 750 °C. This allows the damage initiation, evolution and failure processes to be observed directly. The significant variation in ductility – consistent with the limited number of grain boundaries being present – is rationalised using a crystal plasticity approach calibrated by experiments on single crystals loaded along the <001>, <011>, and <111> directions. Quantitative strength and toughness values for the grain boundaries are estimated using a cohesive zone method. The modelling approach is used to determine an approximation of the size of the representative volume element (RVE) needed for volume-averaged behaviour.

© 2018 The Author(s). Published by Elsevier Ltd on behalf of Acta Materialia Inc. This is an open access article under the CC BY 4.0 license (<http://creativecommons.org/licenses/by/4.0/>).

## 1. Introduction

The grain boundaries of nickel-based superalloys – in common with many polycrystalline alloys – can be their Achilles' heel [1–4]. Grain boundaries can indeed impair the macroscopic response, because they can support crack initiation and hence quasi-brittle behaviour, which is of practical relevance for their application in high temperature systems [3,5–7]. Hence, the local geometry, nature and orientation of a grain boundary with respect to the local stress tensor play a critical role in influencing mechanical properties [8,9]. Many observations in the literature support this [2,10–14]. For instance, it has been shown that localised grain boundary serration can delay crack propagation [10,11]. More particularly, because the orientation of a grain boundary plane changes along its length, voids and cavities forming around the more stressed parts of a grain boundary do not necessarily interlink [12,13], preventing continuous and rapid intergranular crack growth. Other effects, such as environmentally-assisted grain boundary degradation [2,14], are also affected by the local grain boundary architecture. For example, a shorter diffusion path – along grain boundaries which are faceted rather than wavy for

example – can be detrimental to oxidation-assisted cracking [15]. The effect of the atomic scale arrangement at the interfaces has also been studied: alloys with low  $\Sigma$  boundaries show improved ductility and strength [16].

Nonetheless, the research carried out so far is often qualitative: there is a paucity of quantitative information about the properties of grain boundaries in metals and alloys. This is because quantification of the critical interfacial properties – e.g. strength and toughness – is challenging from both numerical and experimental points of view. Experimentally, there is a need to extract quantitative information concerning grain boundary behaviour during deformation. Significant progress has been made with nano- and micro-testing techniques – e.g. micro-cantilever and nano-indentation – to study the behaviour of individual grain boundaries, with some success [17–21]. A difficulty however is that rather reduced volumes of material are employed, which may be insufficient to include all microstructural features, e.g. grain boundary precipitates, so that the properties deduced may not be representative of volume-averaged grain boundary behaviour [22]. Other factors such as the high volume fraction of free-surfaces and the contamination during focused ion beam milling [23,24] may jeopardise the results. Finally, the challenges escalate quickly as the temperature of interest increases – it can be difficult to ascertain the accuracy of the temperature ahead of the loading tip. With these points in mind, a micro-tensile in-situ tensile testing device

\* Corresponding author. Department of Engineering Science, University of Oxford, Parks Road, Oxford, OX1 3PJ, United Kingdom.

E-mail address: [roger.reed@eng.ox.ac.uk](mailto:roger.reed@eng.ox.ac.uk) (R.C. Reed).

such as that used here – which too can be operated in a scanning electron microscope (SEM) – offers some advantages. It provides time-resolved observations of the damage events which arise at the surface of the sample, thus allowing one to identify those factors which contribute to the initiation of the failure process while resolving spatial strains using image correlation techniques [25,26]. From the numerical point of view, there is a need to rationalise and predict the behaviour of grain boundaries using micromechanical models. Over the last years, the use of crystal plasticity finite element modelling has been of growing popularity for the identification of critical local parameters which lead to microstructural damage [27–29]. This method allows the inclusion of deformation heterogeneity by mapping explicitly rather realistic grain structures [30,31]. However, the identification and accurate modelling of damage evolution at grain interfaces is in many ways more challenging. In this regard, cohesive zone modelling can be employed: Needleman [32,33] first combined crystal plasticity modelling with an energy-based fracture criteria which can be employed to simulate grain boundaries. Similar approaches have been used to study damage nucleation phenomena in a number of different material systems [34–37] – these demonstrate the capability of non-local techniques to model mechanical events at the grain boundaries. However, one must keep in mind that the accuracy of these models is often linked intrinsically to the representativeness of the experimentation used for calibration.

In this paper, a method is proposed to measure the mechanical response of individual grains, estimate the properties of the grain boundaries in a polycrystalline nickel-based superalloy and extrapolate the homogenised response of the material accounting for the grain boundary mechanics. The overarching goal is to build a micromechanical model by making use of a crystal plasticity approach coupled with an appropriate treatment of the grain boundaries using cohesive elements. The experimental campaign has necessitated the measurement of the strain-rate and orientation dependency of single-crystal testpieces and the grain-boundary behaviour of bi-crystalline portions of material. The kinematics of damage evolution are elucidated using *in-situ* scanning electron microscope tensile testing of small-scale material volumes; hence as will be demonstrated, the behaviour of individual grain boundaries can be isolated and observed directly. The modelling campaign has required the estimation of the single crystal behaviour and then its use in explicit micromechanical models to elucidate the mechanical response of the grain boundaries. In the final part of the paper, the modelling framework is used to simulate polycrystalline materials – with predictions compared to experimental observations to reinforce confidence in our approach. Our achievement is an accurate and realistic modelling of the high-temperature deformation regime that these kind of alloys experience during service, which accounts for grain boundary behaviour and properties.

## 2. Experimental methods

### 2.1. Material

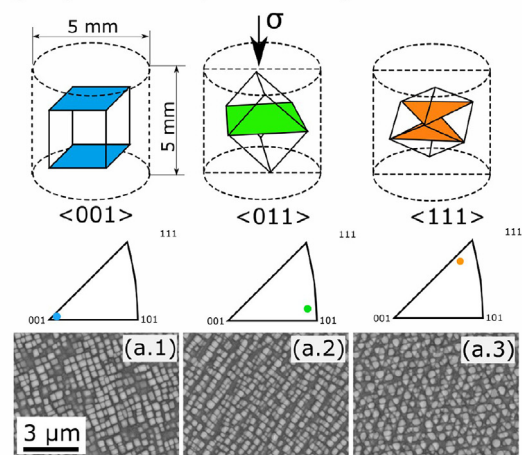
The nickel-based superalloy STAL15 is studied in both its polycrystalline (conventionally casted, CC) and single-crystalline (SX) form, see Table 1. STAL15 is a  $\gamma'$  strengthened alloy originally

developed for power generation applications, but its characteristics are typical of those alloys used in jet engine applications. Particular details about the alloy and its microstructure can be found elsewhere [38]. Cobalt and chromium are present to improve the oxidation resistance, tantalum and aluminium are added to promote hardening by the  $\gamma'$  phase, and molybdenum and tungsten are included to improve the creep strength. In its polycrystalline form, the grain structure is equiaxed with grain size in the range of 700–1200  $\mu\text{m}$ . In its single crystalline form, the alloy has approximately 55%  $\gamma'$  phase with a cuboid distribution – Fig. 1 (a) shows the microstructure for each one of the three SX directions.

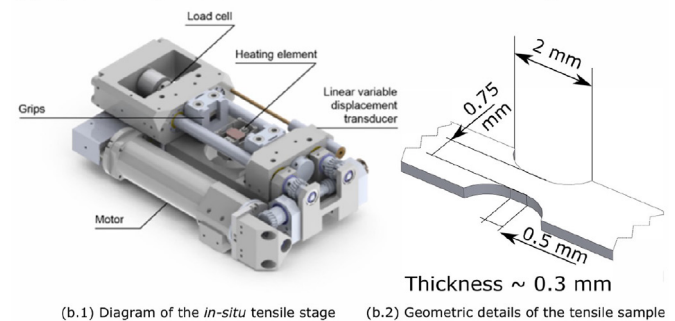
### 2.2. Single-crystalline compression tests

Interpretation of our data requires crystal plasticity modelling,

#### (a) Singlecrystal: SX compression testing in three directions



#### (b) Quasi-bicrystal: Mini-RVE *in-situ* SEM tensile testing



#### (c) Polycrystal: tensile testing of polycrystalline material

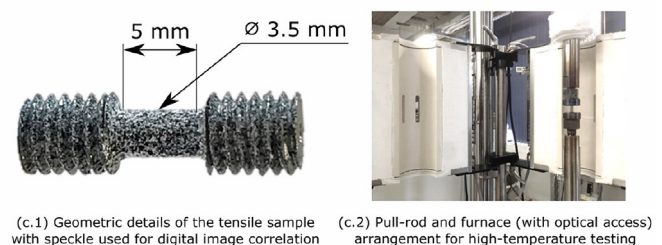


**Fig. 1.** Summary of experimental methods. (a) Single-crystal compression tests showing the employed geometry and the microstructure for: (a.1)  $\langle 001 \rangle$ , (a.2)  $\langle 011 \rangle$  and (a.3)  $\langle 111 \rangle$  loading directions. (b) Diagram of the *in-situ* SEM tensile module and the geometry of the micro tensile sample used to measure quasi bi-crystalline microstructures. (c) Setup and geometry employed to measure the behaviour of polycrystal samples.

**Table 1**

Chemical composition for the STAL15 alloy investigated in this work (at.%).

Alloy	Co	Cr	Mo	W	Al	Ta	Hf	C	B
STAL15-CC	5.50	16.55	0.60	1.21	10.01	2.43	0.02	0.47	0.08
STAL15-SX	5.15	17.21	0.63	1.25	10.03	2.62	0.03	–	–

which in turn needs to be calibrated carefully. For this purpose, cast bars with their longitudinal axes parallel to the  $\langle 001 \rangle$ ,  $\langle 011 \rangle$ , and  $\langle 111 \rangle$  directions – see Fig. 1(a) – were specially commissioned. These were prepared using investment casting and a seeding approach. To measure the single crystal bulk behaviour, constant displacement compression tests were carried out in a servo-electric Instron machine equipped with a 100 kN load cell. Cylinders which measured 5 mm in length and 5 mm in diameter were machined using electro discharge machining (EDM) and ground using 600 grit abrasive paper to remove any induced damaged layer. These were tested under different constant compression speeds:  $1 \times 10^{-4}$ ,  $4 \times 10^{-5}$ ,  $1 \times 10^{-5}$ , and  $4 \times 10^{-6}$  s at a temperature of 750 °C. The samples were positioned between silicon carbide dies with 35 mm diameter and 15 mm thick – these transferred the load from the tested specimen to the superalloy rods. For lubrication, boron nitride spray was applied over the die surface, barrelling was not observed. The strain was controlled using the machine crosshead and measured *via* digital image correlation. For this, the surface of the sample was speckled using high-temperature paint.

### 2.3. In-situ SEM tensile testing of quasi bicrystalline material

Miniaturised sections are tested to establish the behaviour of individual grain boundaries, using an in-situ SEM tensile testing module – illustrated in Fig. 1(b). The approach provides the load-displacement behaviour of the selected section coupled with surface observations of grain boundaries. Specimens of the polycrystalline STAL15 were wire cut using EDM with the geometry shown in Fig. 1(b). A gauge area of  $500 \times 750 \mu\text{m}$  was used and polished down to approximately  $300 \mu\text{m}$  thickness. The material has a mean grain size larger than  $700 \mu\text{m}$ , thus only a handful of grains are present in the reduced gauge section. The samples were prepared for testing and microscopy following the traditional sample preparation techniques. Before testing, the microstructure and crystallographic characteristics were extracted using the electron back-scattered diffraction (EBSD) method.

For imaging, a Zeiss Evo LS1 W-filament SEM equipped with an Oxford Instruments EBSD detector was used. The tests were carried out using a Kammrath and Weiss *in-situ* tensile module. The module was fitted with a resistance heater capable of reaching temperatures up to 1000 °C. A thermocouple was spot-welded to the surface of the sample for temperature monitoring. The samples were tested at a nominal strain rate of  $5 \times 10^{-5}$  s at a temperature of 750 °C. The tests were controlled using the machine crosshead separation as measured by a linear transducer. Micrographs were captured at intervals of approximately 0.5% engineering strain. In order to capture those, the test was paused for approximately 1 min. After image acquisition, the test was resumed using identical displacement-controlled conditions. The surfaces of the samples were ground and polished using colloidal silica and posteriorly speckled using gold nanoparticles in order to allow post-processing *via* digital image correlation.

### 2.4. Polycrystalline tensile tests

Experimentation in polycrystals is used here to validate the approach. For this purpose, isothermal, constant strain-rate tensile tests were carried out using an Instron electro-mechanical testing machine. Tests were carried out at 750 °C using strain rates of  $6.5 \times 10^{-4}$  and  $6.5 \times 10^{-6}$  s. Cylindrical tensile samples with a gauge length of 5 mm and a diameter of 3.5 mm were machined from casting bars of STAL15-CC – the geometry is shown in Fig. 1(c). This figure shows the temperature-resistant speckle used for digital

image correlation. For this purpose, the furnace is equipped with windows to grant *in-situ* optical access to the specimen – see Fig. 1(c). The temperature was monitored and feedback controlled using a thermocouple positioned next to the specimen gauge.

## 3. Numerical methods

The overarching aim is to model the time-dependent viscoplastic behaviour of the polycrystalline nickel-based superalloy using an approach which accounts for grain boundary behaviour. A combination of crystal plasticity theory to capture the single crystal grain bulk behaviour and cohesive zone modelling to represent damage evolution at the grain boundaries is used. The material parameters are calibrated to the experimental data acquired here: (i) single-crystal compression tests for the grain bulk parameters and (ii) quasi bi-crystalline tensile tests for the grain boundary parameters. To illustrate and validate the power of the multiscale model developed here, it has been used to simulate the behaviour of polycrystalline aggregates. This has been used to analyse the localised failure process which evolves in time and leads to a global structural instability.

### 3.1. Single crystal plasticity model

Multiplicative decomposition of the deformation gradient  $\mathbf{F} = \mathbf{F}^p \mathbf{F}^e$  – where  $\mathbf{F}^p$  is the plastic part and  $\mathbf{F}^e$  is the linear elastic part – is employed, following the classical approaches of [39–41]. The evolution of the plastic deformation gradient  $\mathbf{F}^p$  is assumed here to arise solely from crystalline slip – consistent with plastic shear of the material to an intermediate reference configuration. The rate of the plastic velocity gradient  $\mathbf{L}^p$  is defined as the sum of the slipping rate  $\dot{\gamma}^\alpha$  of all the  $\alpha$  slip systems by

$$\mathbf{L}^p = \mathbf{F}^p \mathbf{F}^{p-1} = \sum_{\alpha} \dot{\gamma}^\alpha (\mathbf{s}_0^\alpha \otimes \mathbf{m}_0^\alpha) \quad (1)$$

where  $\mathbf{s}_0^\alpha$  and  $\mathbf{m}_0^\alpha$  are the unit vectors for the slip direction and the normal to the slip plane in the reference configuration respectively. The evolution of texture is written as a function of the elastic deformation gradient as

$$\mathbf{s}_t^\alpha = \mathbf{F}^e \mathbf{s}_0^\alpha \mathbf{m}_t^\alpha = \mathbf{m}_0^\alpha \mathbf{F}^{e-1} \quad (2)$$

where  $\mathbf{s}_t^\alpha$  and  $\mathbf{m}_t^\alpha$  are the slip direction and the normal to the slip plane in the deformed configuration.

The plastic multiplier  $\dot{\gamma}^\alpha$  in a slip system  $\alpha$  is a direct function of the current projected stress  $\mathbf{S}$  and is defined using a power-law dependency consistent with

$$\dot{\gamma}^\alpha = \dot{\gamma}_0 \left| \frac{\tau^\alpha}{\tau_c^\alpha} \right|^{\frac{1}{m}} \text{sgn}(\tau^\alpha) \quad (3)$$

where  $\dot{\gamma}_0$  is a time constant,  $m$  is the strain rate sensitivity parameter,  $\tau_c^\alpha$  is the critical resolved shear stress, and  $\tau^\alpha$  is the resolved shear stress expressed as

$$\tau^\alpha = \mathbf{C} \mathbf{E}^e : (\mathbf{s}_0^\alpha \otimes \mathbf{m}_0^\alpha) \quad (4)$$

where  $\mathbf{C}$  is the fourth-order stiffness tensor and  $\mathbf{E}^e$  is the Green-Lagrange strain tensor. The strain hardening is introduced *via* the evolution rate of the critical resolved shear stress following



$$\dot{\gamma}_c^\alpha = \sum_\beta h_{\alpha\beta} \left| \dot{\gamma}_\beta^\alpha \right| \quad (5)$$

where  $h_{\alpha\beta}$  are the slip hardening moduli due to self and latent hardening. The self hardening moduli  $h_{\alpha\alpha}$  can be expressed following [42,43] as

$$h(\gamma) = h_{\alpha\alpha} = h_0 \text{sech}^2 \left| \frac{h_0 \gamma}{\tau_s - \tau_0} \right| \quad (6)$$

where  $h_0$  is the initial hardening modulus,  $\tau_0$  is the yield stress,  $\tau_s$  is the stage I stress and  $\gamma$  is the accumulated shear strain over all slip systems expressed as

$$\gamma = \sum_\alpha \int_0^t \left| \dot{\gamma}_\alpha^\alpha \right| dt \quad (7)$$

The latent hardening moduli follows

$$h_{\alpha\beta} = qh(\gamma) \quad (8)$$

where  $q$  is an interaction coefficient and  $h(\gamma)$  is defined in Eq. (6).

### 3.2. Grain boundary damage model

In our simulations, cracks are assumed to be generated at grain interfaces exclusively; intragranular cracking is not considered since it is not often observed under the conditions of temperature and strain-rate of interest here. Cohesive zone modelling is used [44–46]. Although the approach cannot replicate micro-scale processes, it is effective when modelling stochastic aspects of failure. For example, the method can predict how shear and stress localisation – which may appear under certain grain boundaries – develop into damage sites which will eventually become a crack path [47,48]. Here, the behaviour of the grain boundary is assumed purely elastic until damage begins. When damage starts – based on a damage initiation criteria – the bulk elastic modulus is reduced, thus reducing the stress following

$$t_i = (1 - d_i) K_i \delta_i \quad (9)$$

where  $K_i$  is the stiffness,  $t_i$  is the traction,  $\delta_i$  the separation, and  $i$  is the characteristic mode of deformation ( $i = I, II$  for mode I and mode II respectively). In the present work, it is assumed that the grain boundaries follow a trapezoidal traction-separation law (TSL) – GBs are allowed to deform *plastically* before softening occurs – see Fig. 2(b). In mode II, this plastic plateau is used to model the grain boundary sliding effect. The energy release rate of mode II fracture is assumed larger than mode I, thus, GBs can deform tangentially free of damage, usually until mode I fracture occurs. The damage parameter of the TSL is defined following

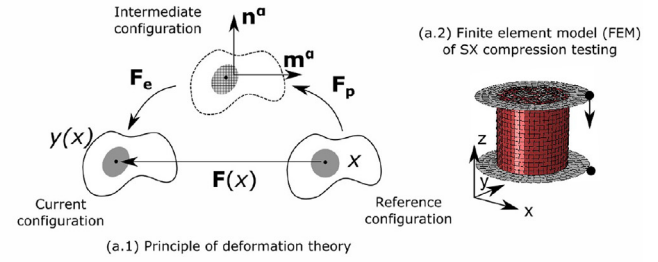
$$d_i = 1 - \frac{\delta_{1,i}}{\delta_i} \quad (10)$$

where  $\delta_{1,i}$  is the damage initiation separation defined as  $\delta_{1,i} = t_i^0 / K_i$ , and  $\delta_i$  is the current separation. In the softening part of the curve, the damage parameter is defined as

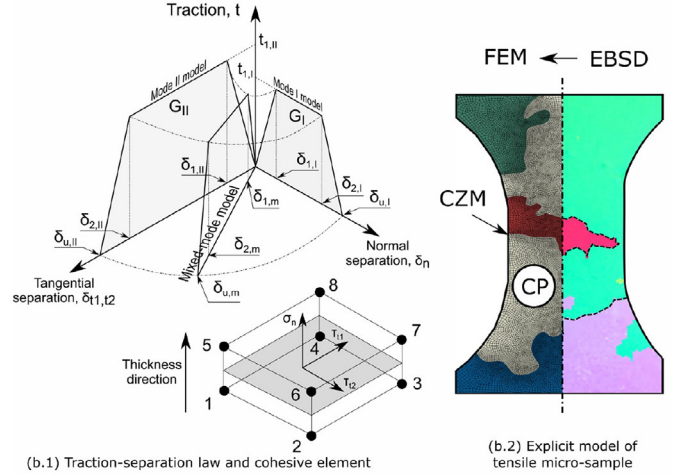
$$d_i = 1 - \frac{\delta_{1,i}(\delta_{u,i} - \delta_i)}{\delta_i(\delta_{u,i} - \delta_{2,i})} \quad (11)$$

where  $\delta_{2,i}$  is the separation which determines the end of the

### (a) Singlecrystal: crystal plasticity (CP) modelling



### (b) Quasi-bicrystal: CP + cohesive zone modelling (CZM)



### (c) Polycrystal: CP + CZM + Synthetic polycrystal generation

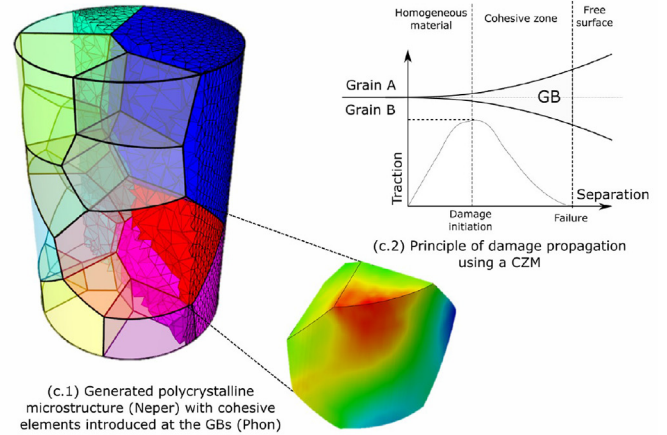


**Fig. 2.** Summary of numerical methods. (a) Single-crystal crystal plasticity modelling with finite element model for SX compression tests. (b.1) The trapezoidal softening law for mode I, mode II, and mixed-mode – showing the nature of each fracture mode and indicating the nomenclature for the used TSL. (b.2) Explicit FE representation of a quasi bi-crystalline tensile sample. (c) Generated polycrystalline microstructure and principle of damage initiation and propagation of the cohesive elements introduced at the grain boundaries.

plateau in each mode, and  $\delta_{ui}$  is the final separation. The final separation is obtained as a function of the critical fracture energy  $G_i^c$  which is equivalent to the total area under the TSL curve for each mode. Thus, the separation at failure is defined following



$$\delta_{u,i} = \frac{2G_i^C}{t_{1,i}} + \delta_{1,i} - \delta_{2,i} \quad (12)$$

where  $t_{1,i}$  is the maximum traction in each mode. Since grain boundaries have arbitrary orientations in a polycrystalline microstructure, the cohesive elements will be subjected to mixed-mode behaviour. A mixed-mode damage criterion is thus formulated using the quadratic stress criterion which follows

$$\left(\frac{t_I}{t_{1,I}}\right)^2 + \left(\frac{t_{II}}{t_{1,II}}\right)^2 = 1 \quad (13)$$

where  $t_{1,I}$  and  $t_{1,II}$  are the maximum traction values in mode I and mode II respectively. The above is true given that the normal stress  $t_I$  is positive – compression does not initiate damage. This criterion can be written as a function of separation values as

$$\left(\frac{\delta_I}{\delta_{1,I}}\right)^2 + \left(\frac{\delta_{II}}{\delta_{1,II}}\right)^2 = 1. \quad (14)$$

Defining an equivalent mixed-mode separation  $\delta_m = \sqrt{\delta_I^2 + \delta_{II}^2}$  and a mixed mode ratio  $\beta = \delta_{II}/\delta_I$ , the mixed-mode separation for the damage initiation is

$$\delta_{1,m} = \delta_{1,I}\delta_{1,II}\sqrt{\frac{1+\beta^2}{\delta_{1,II}^2 + \beta^2\delta_{1,I}^2}}. \quad (15)$$

Analogously, the separation which determines the end of the mixed-mode plateau  $\delta_{2,m}$  can be determined following

$$\delta_{2,m} = \delta_{2,I}\delta_{2,II}\sqrt{\frac{1+\beta^2}{\delta_{2,II}^2 + \beta^2\delta_{2,I}^2}} \quad (16)$$

where  $\delta_{2,i}$  is the separation which marks the end of the plastic zone and is defined as  $\delta_{2,i} = \delta_{1,i} + f_{G,i}G_i^C/t_{1,i}$  where  $f_{G,i}$  is parameter which determines the shape of the TSL curve and must take a value between 0 and  $1 - t_{1,i}/(2G_i^C K_i)$  – where 0 would result in a bilinear TSL. The growth of the crack is controlled by a linear fracture criterion defined as

$$\frac{G_I}{G_I^C} + \frac{G_{II}}{G_{II}^C} = 1 \quad (17)$$

where  $G_I^C$  and  $G_{II}^C$  are the critical energies for mode I and mode II respectively. When Eq. (17) is satisfied, the stresses in the cohesive element are entirely released and the crack is considered fully open. The energy for mixed-mode can be obtained using

$$G_i^C = \frac{t_{m,i}}{2} (\delta_{2,m} - \delta_{1,m} + \delta_{u,m}). \quad (18)$$

Then, the separation upon failure for mixed-mode can be obtained as

$$\delta_{u,m} = \frac{2G_I^C G_{II}^C (1 + \beta^2) - \delta_{1,m} (\delta_{2,m} - \delta_{1,m}) (K_I G_{II}^C + \beta^2 K_{II} G_I^C)}{\delta_{1,m} (K_I G_{II}^C + \beta^2 K_{II} G_I^C)} \quad (19)$$

where  $K_I$  and  $K_{II}$  are the stiffnesses for mode I and II. Finally, using the equivalent mixed-mode displacement, the damage variable  $D$  can be fully defined following

$$D = \begin{cases} 0 & \delta_m \leq \delta_{1,m} \\ 1 - \frac{\delta_{1,m}}{\delta_m} & \delta_{1,m} < \delta_m \leq \delta_{2,m} \\ \frac{\delta_{1,m}(\delta_{u,m} - \delta_m)}{\delta_m(\delta_{u,m} - \delta_{2,m})} & \delta_{2,m} < \delta_m \leq \delta_{u,m} \\ 1 & \delta_m > \delta_{u,m} \end{cases} \quad (20)$$

which then can be used to update the stresses in the element directions following

$$\sigma_{t1} = E_t(1 - D)\varepsilon_{t1} \quad (21)$$

$$\sigma_{t2} = E_t(1 - D)\varepsilon_{t2} \quad (22)$$

$$\sigma_n = \begin{cases} E_n(1 - D)\varepsilon_n & \delta_n > 0 \\ E_n\varepsilon_n & \text{else} \end{cases} \quad (23)$$

where the tangential and normal elastic modulus are  $E_t = K_t/t_{\text{element}}$  and  $E_n = K_n/t_{\text{element}}$  respectively. The strains are defined as a function of the separation as  $\varepsilon_{t1,2} = \delta_{t1,2}/t_{\text{element}}$  and  $\varepsilon_n = \delta_n/t_{\text{element}}$  for the tangential and normal direction respectively. The term  $t_{\text{element}}$  is the thickness of the cohesive element – when zero thickness elements are used, a thickness of unity is assumed. The model was implemented into Abaqus using a UMAT user subroutine.

### 3.3. Finite element models of the different microstructural scales

Representative finite element models are used to simulate the microstructures at different testing scales: (i) single crystal compression, (ii) miniaturised quasi bicrystalline tension, and (iii) polycrystalline tension. Fig. 2 shows the geometry of each one of the three finite element models.

For the simulation of single crystal compression tests, eight-node linear brick elements (C3D8) were employed. Approximately 10,000 elements were used to represent the compression specimens – see Fig. 2(a). The crystallographic orientation was assigned accordingly for each of the three loading cases. The specimen is allowed to move freely between the compression dies – these were discretised using rigid elements. A friction coefficient of 0.2 was used to model tangential surface behaviour. The displacement of the rigid dies was imposed so that the reaction force can be used to derive the overall mechanical response so that it can be compared to the experiments for parameter calibration.

For the miniaturised quasi-bicrystalline sections, the grain structure as extracted from the EBSD analysis was modelled explicitly – it was assumed that the microstructure can be extruded along the reduced sample thickness. The corresponding Euler angles for the average crystallographic orientation of each grain were obtained using the EBSD technique. For modelling the grain bulk, eight-node quadrilateral brick elements (C3D8) were employed. The surface mesh of a miniaturised specimen is shown in Fig. 2(b). At the grain boundaries, cohesive contact was defined. Approximately 600,000 elements were used to model each sample. Displacement conditions were assigned to both ends of the gauge section – constant displacement rate was imposed parallel to the tensile axis while the perpendicular direction was constrained. The reaction forces associated to these nodes were used to extract the homogenised mechanical response of the quasi-bicrystal structures.

The polycrystalline microstructure was generated using Neper [49], an open source project which employs Voronoi tessellations to

generate representative microstructures. A gauge length cylinder of 3.5 mm in diameter and 5 mm in length was filled with equiaxed grains with an approximate mean equivalent diameter of 900  $\mu\text{m}$ . Approximately 150,000 elements were used to represent the whole volume – tetrahedron linear elements C3D4 were employed. The crystallographic orientation of each grain was assigned in a random manner. For the grain boundaries, 6-node three-dimensional cohesive elements COH3D6 were generated using Phon [50]. Constant displacement rates were imposed to the external faces of the model mimicking the experimental loading case. Details of a generated synthetic microstructure is shown in Fig. 2(c).

## 4. Results and discussion

### 4.1. Single-crystal compression results for model calibration

Before modelling quasi-bicrystalline structures, the behaviour of the single-crystal needs to be determined. For this purpose, compression experiments are used: experimental curves for the single-crystal samples tested at 750°C under the loading directions  $\langle 001 \rangle$  and  $\langle 111 \rangle$  at a strain rate of  $1 \times 10^{-4}$ ,  $4 \times 10^{-5}$ ,  $1 \times 10^{-5}$ , and  $4 \times 10^{-6}$  s are shown as data points in Fig. 3(a) and (b) respectively. These curves have been used to calibrate the crystal plasticity

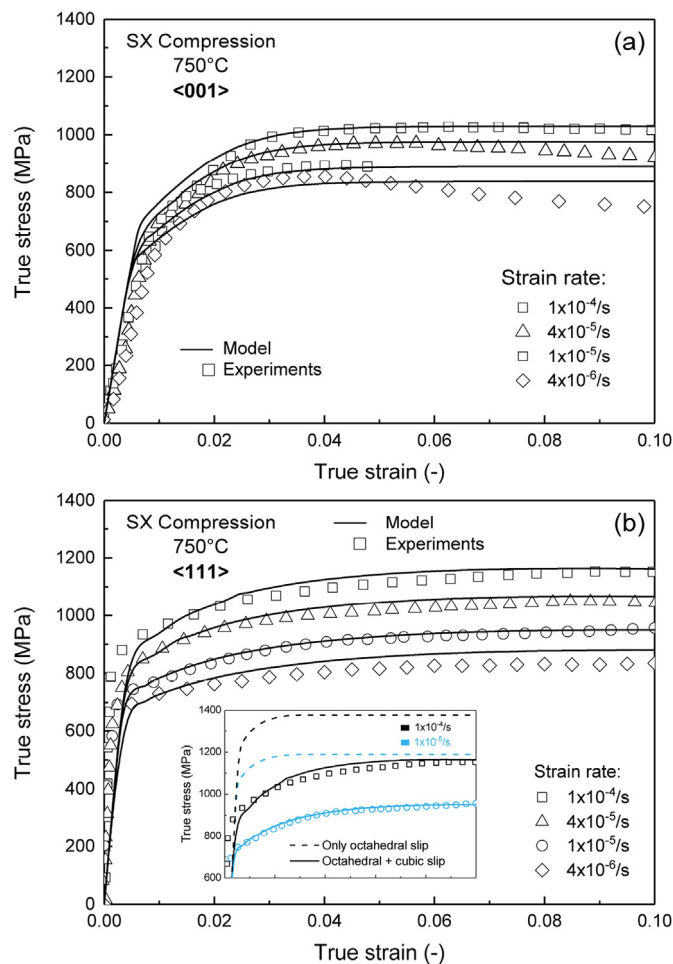


**Fig. 3.** Experimental and numerical modelling results for: (a)  $\langle 001 \rangle$  loading direction, and (b)  $\langle 111 \rangle$  loading direction at 750°C and different strain rates. Symbols show experimental results while solid lines show the crystal plasticity modelling results when combining the contribution between octahedral and cubic slip. The response of pure octahedral slip is shown as dashed lines in the subfigure (b).

model. The first assumption is that the deformation is accommodated by the octahedral slip system  $\langle 011 \rangle \{111\}$  – these usually have the lowest critically resolved shear stress. However, looking at the comparative study shown in Fig. 3(b) for  $\langle 111 \rangle$ , one quickly notices that the strength at this temperature cannot be explained exclusively with slip along octahedral planes – i.e. the strength in the loading direction  $\langle 111 \rangle$  should almost double that of the loading direction  $\langle 001 \rangle$ . The dashed lines presented in the subfigure 3(b) shows the prediction of the crystal plasticity model when one uses exclusively octahedral slip calibrated to the  $\langle 001 \rangle$  loading direction – there is a significant variation between the measured and predicted flow stress for  $\langle 111 \rangle$  loading.

This means either that the material follows a non-Schmidian rule or that there is another slip system active. Conveniently, it has previously been reported that octahedral dislocations crossslip between  $\{111\}$  slip planes or collinear annihilation between dislocations with the same Burgers vector gliding on different planes in the  $\gamma$  phase can explain lower strength values when loading in the  $\langle 111 \rangle$  direction [51,52]. Using a crystal plasticity framework, this effect can be included by incorporating cubic slip [53]. Table 2 shows the Schmid factors (SF) for each possible slip plane (both octahedral and cubic systems) for each loading case: their combination gives a clear indication of which slip system is dominant for each crystal orientation. Since the loading direction  $\langle 001 \rangle$  is accounted by octahedral slip exclusively, the  $\langle 001 \rangle$  experimental results are used to calibrate the model parameters of octahedral slip. Then, experimental results for the  $\langle 111 \rangle$  loading direction are used to calibrate parameters related to cubic slip. Experimental results for the loading direction  $\langle 011 \rangle$  are used to validate the crystal constitutive law.

The material parameters were initially identified assuming perfect uniaxiality – a simple solution could be obtained analytically, thus allowing faster parameter looping to find an optimal solution. After that, the model was refined using a finite element model of the compression tests. This allowed to account for the effect of crystallographic rotation during plastic deformation, local non-uniaxialities within the sample, and friction on the parameter identification process. The results of the model calibration are shown as solid lines in Fig. 3(a) and (b). Fig. 4 shows the experimental points and model results for the  $\langle 011 \rangle$  loading direction at  $1 \times 10^{-5}$  s as a validation exercise. Table 3 shows the calibrated crystal plasticity model parameters. The elastic constants  $C_{11}$ ,  $C_{12}$ , and  $C_{44}$  are approximately 230, 180, and 110 GPa respectively. With the behaviour of the crystal bulk determined and modelled, the attention is now focused on the grain boundaries – the aim is first to better understand their effect on the mechanical properties and then to quantify their behaviour in terms of strength and toughness. This means that from this section onwards the parameters of the crystal plasticity model will remain untouched.

**Table 2**

Schmid factors (SF) and number of active slip planes for the set of slip systems  $\langle 011 \rangle \{111\}$  and  $\langle 011 \rangle \{001\}$  when loading on the tensile directions  $\langle 001 \rangle$ ,  $\langle 011 \rangle$  and  $\langle 111 \rangle$ .

Tensile axis	$\langle 011 \rangle \{111\}$		$\langle 011 \rangle \{001\}$	
	No. slip planes	SF	No. slip planes	SF
$\langle 001 \rangle$	8	0.4082	6	0.0
	4	0.0		
$\langle 011 \rangle$	4	0.4082	4	0.3536
	8	0.0	2	0.0
$\langle 111 \rangle$	6	0.2722	3	0.4714
	6	0.0	3	0.0

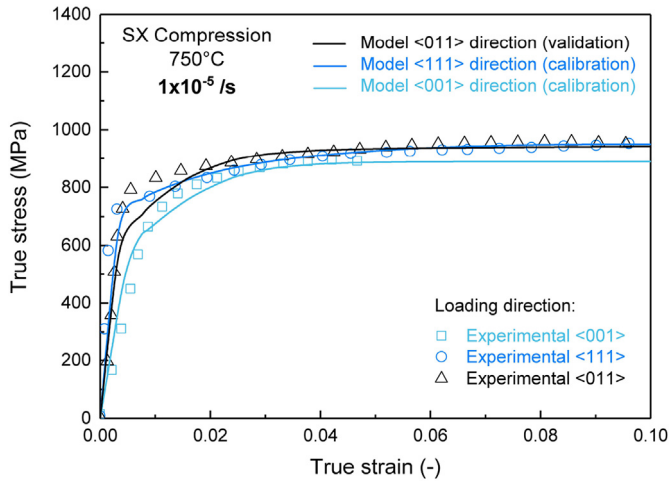


**Fig. 4.** Experimental and numerical modelling results for the <001>, <011> and <111> loading directions tested at a strain rate of  $1 \times 10^{-5}$ /s. <011> used as validation.

**Table 3**

Calibrated crystal plasticity model parameters for both octahedral and cubic slip systems.

	$\dot{\gamma}_0$ (1/s)	$m$	$\tau_s$ (MPa)	$\tau_0$ (MPa)	$h_0$	$q_{\alpha\beta}$
Octahedral	$5.5 \times 10^{-9}$	0.064	230	160	1900	1
Cubic	$2.4 \times 10^{-8}$	0.086	265	210	500	1

#### 4.2. Tensile behaviour of miniaturised quasi-bicrystalline microstructures

Fig. 5 shows the measured stress-strain data for the quasi-bicrystalline specimens. It has been found that these can be divided – on the basis of the ductility characteristics found – into three groups: (i) a first group (A) is formed by those samples with the lowest strength and ductility – those which have an ultimate tensile strength of approximately 700 MPa and reach critical failure below 3% plastic strain. EBSD analyses show that those samples have a main grain boundary perpendicular to the tensile direction and are situated close to the center of the gauge length; (ii) a second group (B) which shows higher values of strength ( $\approx 800$  MPa) and an improvement in the energy release rate to failure. This increase in mechanical properties is believed to be caused by the relative angle of the main grain boundary: by being so inclined, the projected normal stress on the interface is smaller than the macroscopic load applied in the tensile axis; (iii) the third and final group (C) shows the highest values in UTS and strain-to-failure: increasing to approximately 900 MPa and to a maximum strain of  $\approx 6\%$ . Since these samples in the last group do not have a grain boundary (GB) positioned right across the middle of the sample, the macroscopic load and energy necessary to induce damage is increased. In the following sections, the behaviour of each one of these is analysed and modelled in detail. The misorientation of the tested grain boundaries tends to be highly random, there is no indication that the different observed strengths are determined by the differences in grain boundary angle, however, more tests with different misorientations (particularly with low angle grain boundaries) would be necessary to quantify this effect.

#### 4.3. In-situ observations of grain boundary damage

In-situ SEM images are used to elucidate the process of damage and failure of a series of non-RVE samples. Experimental

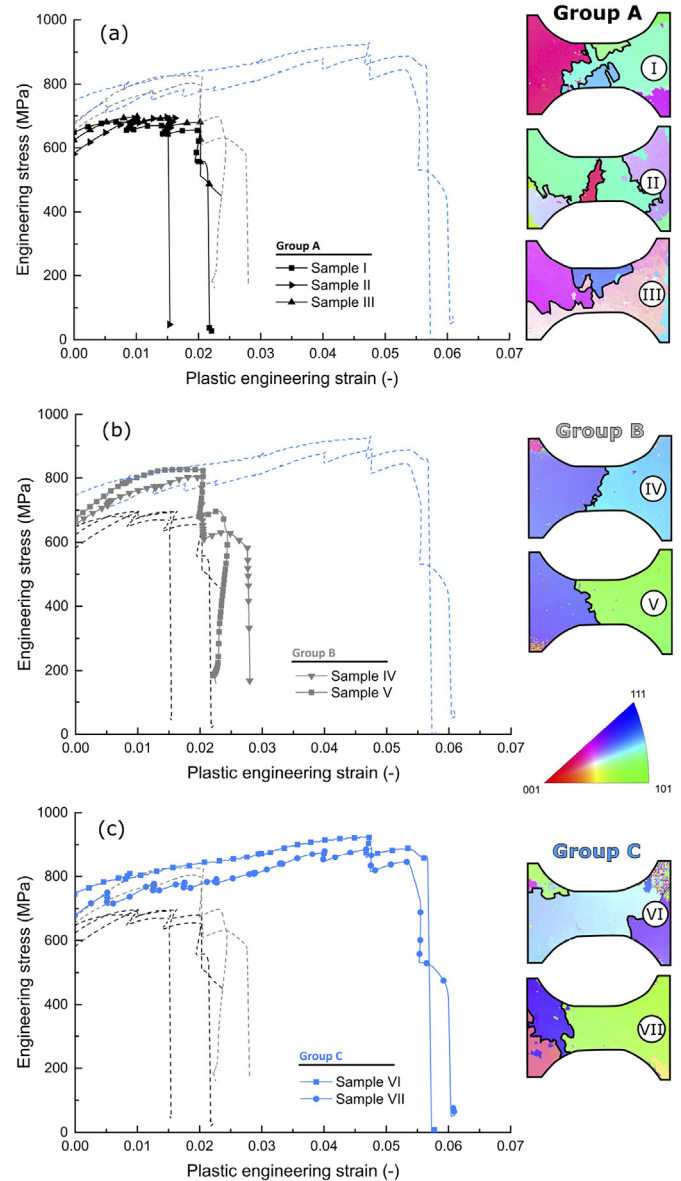


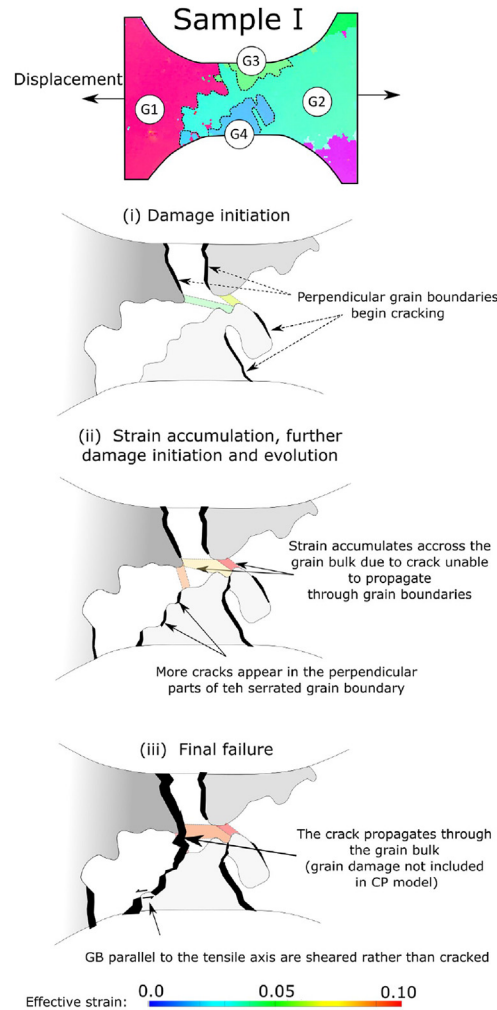
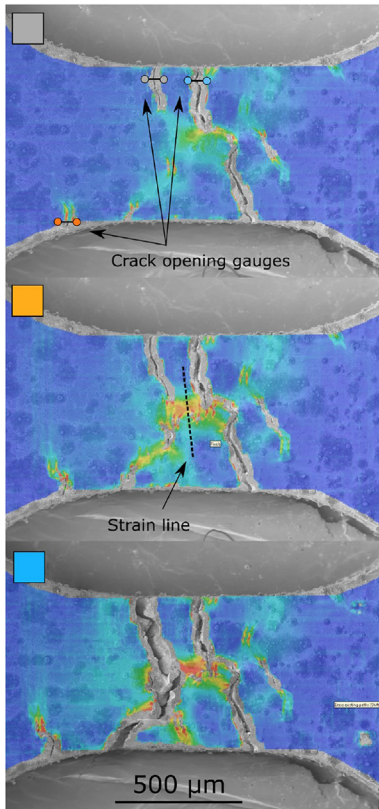
**Fig. 5.** EBSD images of the tested quasi-bicrystalline specimens together with the experimental stress-strain curves for each one of the samples, divided based upon the characteristics of their mechanical behaviour and their grain boundary architecture.

observations are supported by our modelling – the particulars of the cohesive laws to represent GB damage and their calibration are explained later in the section.

Fig. 6 shows the damage events in a first sample, Sample I. The microstructure is shown as an EBSD micrograph at the top of the figure. The crystallographic orientation in terms of Euler angles and GB misorientation is shown in Tables 4 and 5. Experimental observations, overlaid with a two-dimensional strain map derived using digital image correlation, are exposed in the left-hand side of the figure. The images in the right-hand side show the simulated behaviour after calibrating the GB parameters – which is discussed later. From the first set of images – those taken at the lowest strains – it is clear that damage initiates at the grain boundaries more perpendicular to the loading axis. Indeed, one may correlate the crack initiation at the GB with the *plastification* of the macroscopic stress behaviour – evidence suggests that the observed yielding is an effect of the GB damage. This behaviour is captured by the



### Experimental: in-situ SEM images



### Model: crystal plasticity with cohesive boundaries

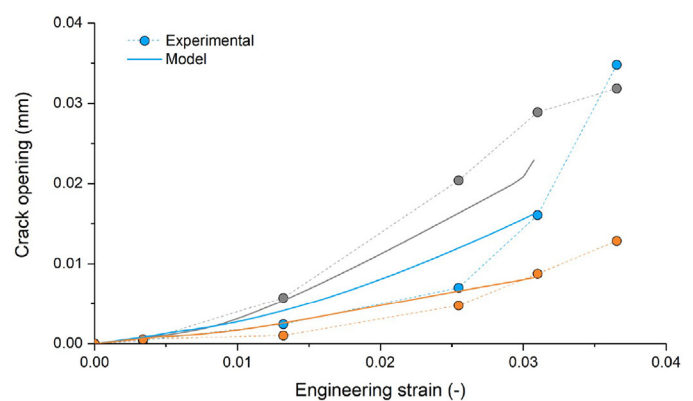
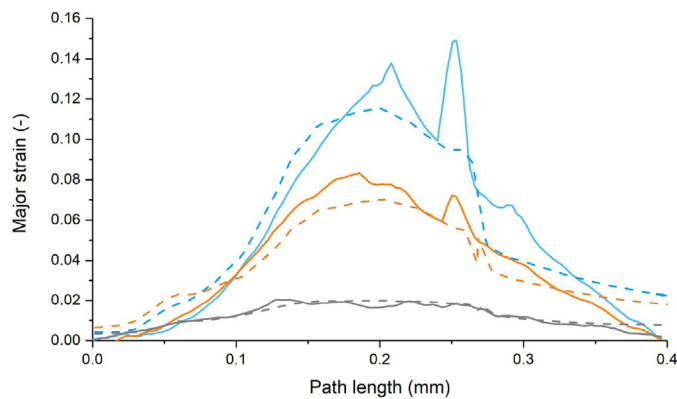
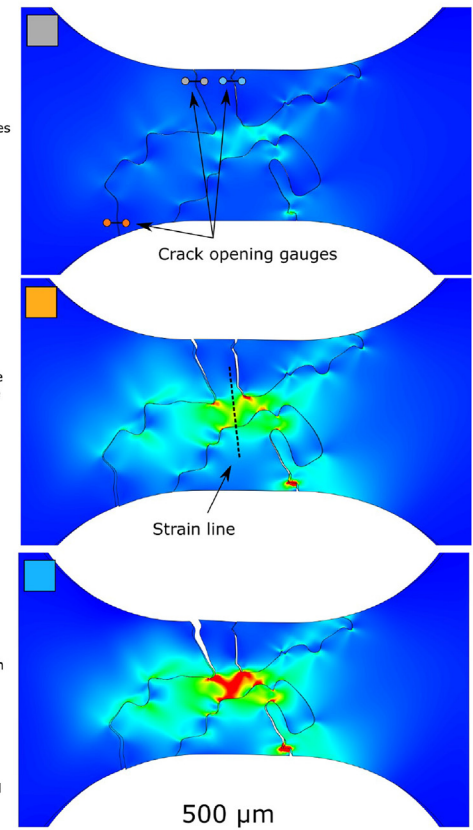


**Fig. 6.** Deformation and damage sequence for Sample I. Left-hand side: *in-situ* experimental observations of the sample surface during testing with an overlay of the principal strain derived using DIC. Right-hand side: modelling results showing strain accumulation in the grain lattice and partial decohesion of the grain boundaries. Lower part: Graphs comparing strains across the selected path line and crack opening length.

model. As the deformation continues, the crack at the grain boundaries is locked by those grain boundaries oriented  $>45^\circ$ . This introduces a plateau in the stress-strain curve as damage is halted and bulk strain begins to accumulate. Since the decohesion of the grain boundary is not homogeneous, the pinned GBs serve as initiation sites for bulk strain localisation. Again, this is observed in both experiments and models. Right before failure, almost all GBs have cracked and opened – except those oriented parallel to the

loading axis which are still shearing. Once the strain in the bulk of the grain reaches a critical value, transgranular failure occurs and final macroscopic failure is observed. Obviously, this is not observed in the model since bulk damage is not considered. In the lower part of Fig. 6, the localisation of strain between experiment and model is compared – see highlighted path line. Results show a good agreement for each of the selected time points. Moreover, crack gauges which measure the opening of grain boundaries show that

**Table 4**

Average crystallographic orientation in Euler angles for the grains in each of the modelled *in-situ* samples.

Sample No.	Grain ID	$\Phi 1$ (°)	$\Phi$ (°)	$\Phi 2$ (°)
Sample I	G1	214	12.9	135.25
	G2	324.6	43.5	72.16
	G3	61.2	38.9	258.82
	G4	344.6	44.9	27.79
Sample II	G1	124.6	45.18	254.3
	G2	206.16	11.14	143.24
	G3	74.86	32.57	328.67
	G4	69.18	34.64	333.92
Sample VII	G1	136.58	18.67	241.12
	G2	220.66	46.65	136.62
	G3	327.23	34.22	354.80

**Table 5**

Summary of grain boundary misorientation angle for each of the modelled *in-situ* samples.

Sample No.	Grain boundary ID (Grain pair)	Misorientation (°)
Sample I	GB1 (G1–G2)	57.1
	GB2 (G2–G3)	44.8
	GB3 (G2–G4)	33.0
Sample II	GB1 (G1–G2)	55.6
	GB2 (G1–G3)	50.2
	GB3 (G1–G4)	47.2
Sample VII	GB1 (G1–G2)	55.0
	GB2 (G2–G3)	44.2

the model captures the trend observed experimentally.

The behaviour observed in sample II is similar – see Fig. 7. However, in this case, the GB crosses the whole gauge area approximately perpendicular to the loading axis. This leads to a decrease in the strain-to-failure. Nevertheless, the damage sequence is analogous: (i) damage appears during the elastic loading around the most critical GBs – those located in the top right-hand side corner of the sample and those right in the middle of the gauge, (ii) the damage expands along the central GB and bulk straining occurs around locked GBs until the final failure is reached. The model is able to capture both the damage initiation locations

and the GBs which cause the final failure: this strengthens the validity of both the experimental observations and the modelling strategy.

The behaviour of samples such as Sample VII is different. In this case, there is no GB situated right across the gauge area. There is a difference in the observed macroscopic behaviour but also a different sequence of damage – see Fig. 8. Similarly to samples I and II, damage initiates at those GBs perpendicular to the loading axis and closer to the sample center where stresses are higher. However, after this, the normal stresses in the rest of the boundaries, as projected on their relative orientations, are not large enough for damage to continue. Once the GB crack is locked, significant intragranular straining occurs. This accumulation of intragranular strain is predicted by the model – it is dependent on the active slip planes and on the geometrical inhomogeneity introduced by the partial decohesion. As deformation continues, the higher levels of strain cause intragranular cracking. Although this kind of damage is not considered in the models, the areas where those cracks appear are indeed areas where the highest accumulation of strain is observed – see areas marked in the drawings. This shift from GB cracking to intragranular deformation is believed to be responsible for the increase in ductility and strength. The final failure is a combination of the initial grain boundary failure and the intragranular damage induced later. Finally, analogous to the comparison introduced previously, the lower graphs in Fig. 8 compare the simulated and experimental strains along three critical locations with high gradients of strain. Results show good agreement between both. Moreover, the results show that the model is able to capture the opening of the critical grain boundary situated in the middle of the sample – that which induces the initial damage.

#### 4.4. Cohesive zone modelling for grain boundary mechanics

The models and experiments presented above were used to estimate the mechanical properties of the grain boundaries, specifically their maximum traction and fracture toughness. Also, one can quantify, to what extent, the mechanical behaviour of the material is limited by the GBs themselves.

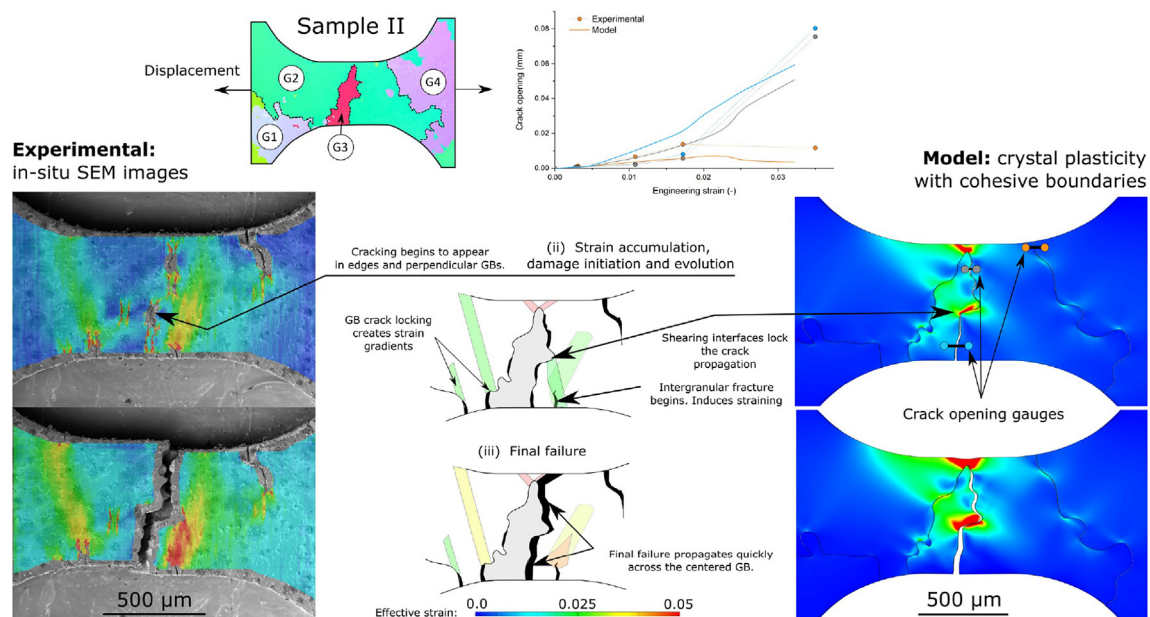


**Fig. 7.** Deformation and damage sequence for Sample II. Left-hand side: *in-situ* experimental observations of the sample surface during testing with an overlay of the principal strain derived using DIC. Right-hand side: modelling results showing strain accumulation in the grain lattice and partial decohesion of the grain boundaries.



### Experimental: in-situ SEM images

### Model: crystal plasticity with cohesive boundaries

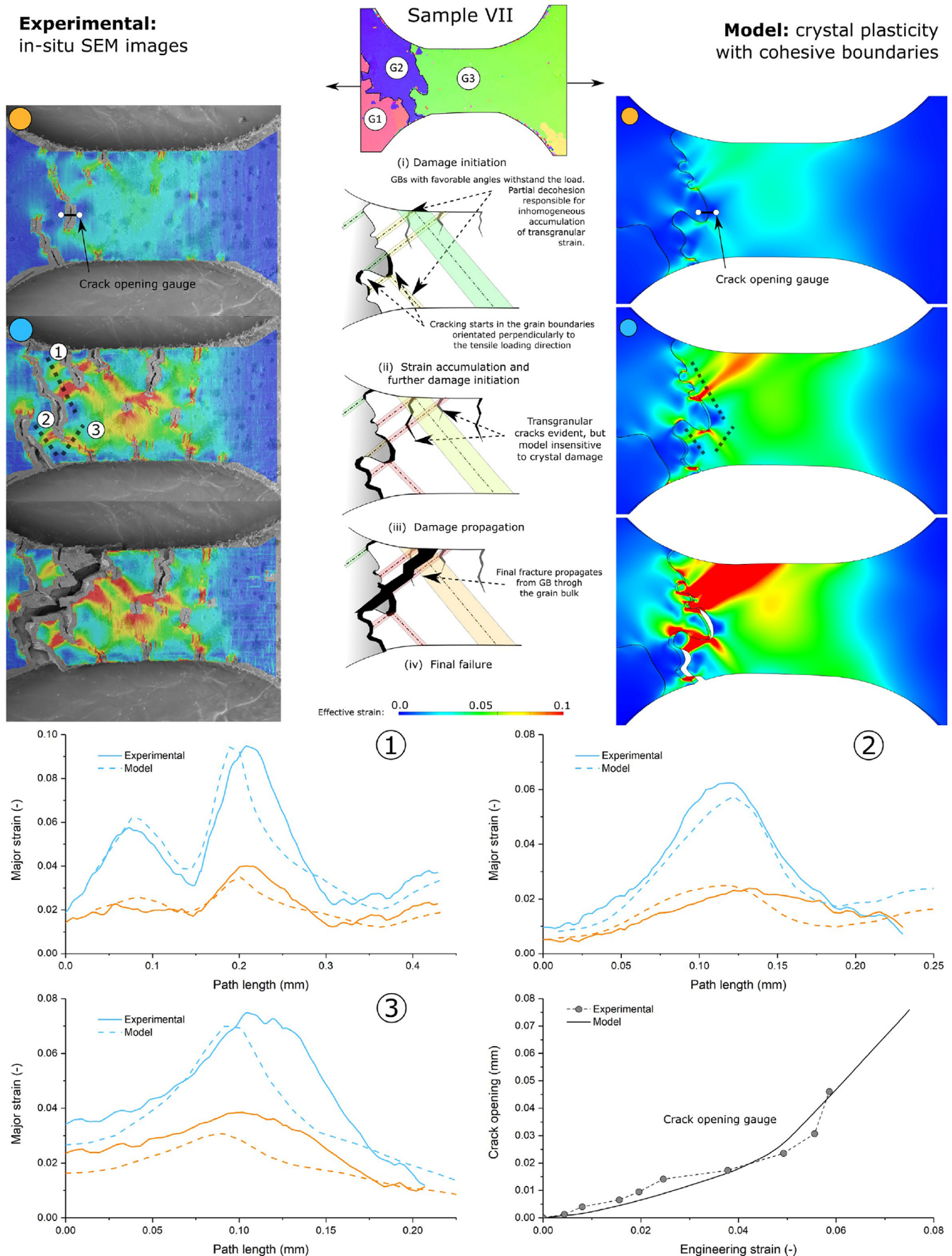


**Fig. 8.** Deformation and damage sequence for Sample VII. Left-hand side: in-situ experimental observations of the sample surface during testing with an overlay of the principal strain derived using DIC. Right-hand side: modelling results showing strain accumulation in the grain lattice and partial decohesion of the grain boundaries. Lower part: Graphs comparing strains across the selected path lines and crack opening length.



### Using CZM to determine grain boundary properties

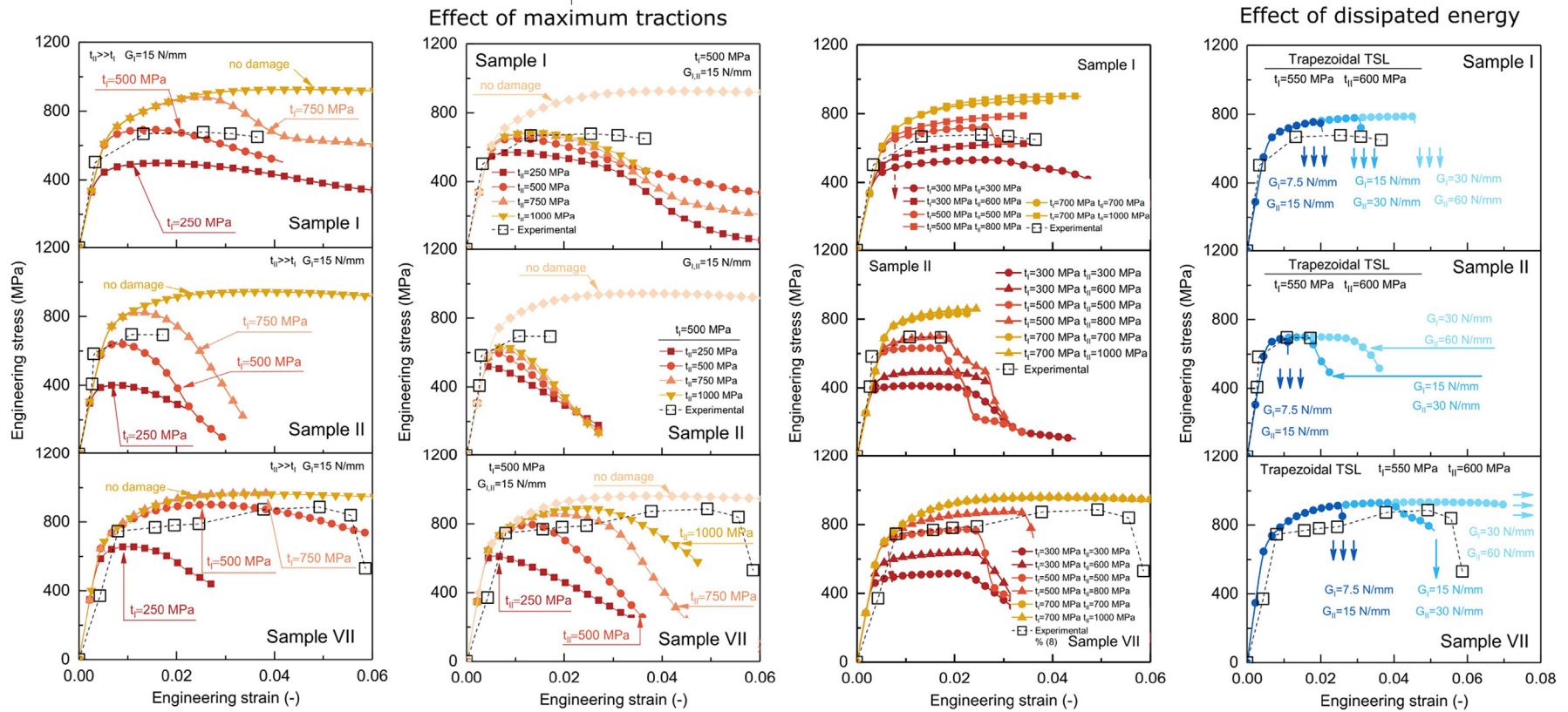
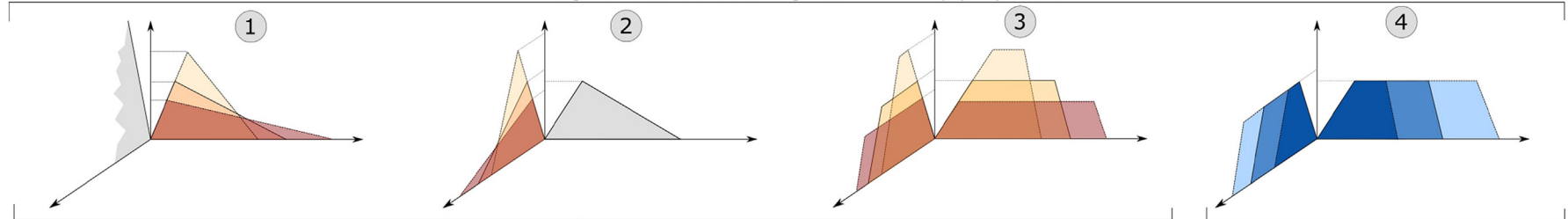


**Fig. 9.** Predicted mechanical behaviour using the explicit bicrystalline models using different mechanical properties for the interface elements. Experimental data is shown as scattered points, in this case, the strain was derived directly from experimental image sequence. Right-hand side shows the calibrated TSL which better represents the behaviour of the grain boundary.

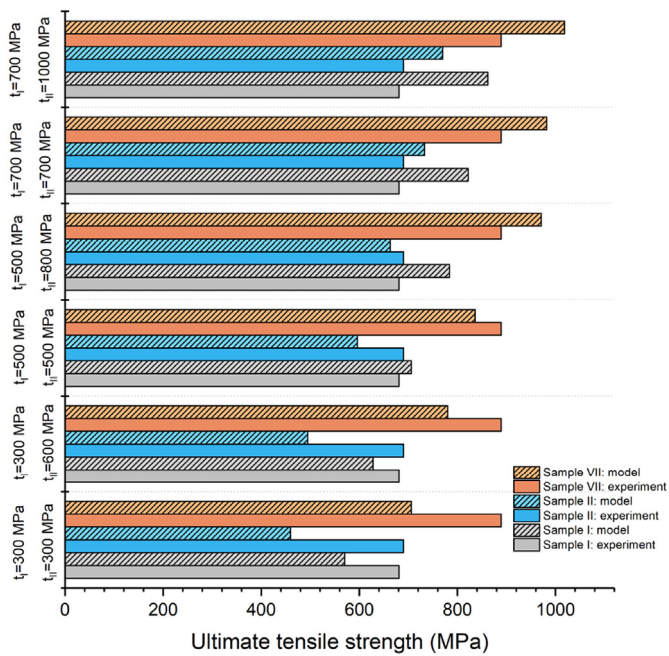


Fig. 10. Comparison between the predicted ultimate tensile strength values and the experimental measurements for different values of the trapezoidal TSL.

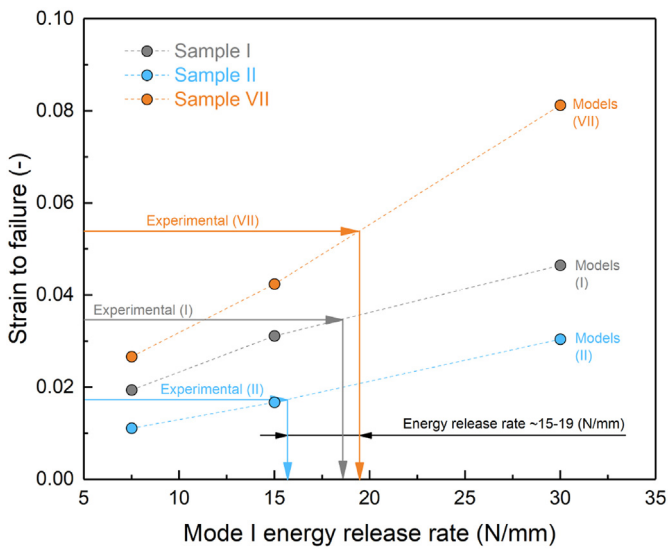


Fig. 11. Comparison between the predicted strain-to-failure values and the experimental measurements for different energy release rate values.

**Table 6**  
Cohesive properties of the grain boundaries as calibrated in Fig. 9.

$t_{1,I}$	$t_{1,II}$	$G_I^C$	$G_{II}^C$	$f_{G,I,II}$	$K_{I,II}$
(MPa)	(MPa)	(N/mm)	(N/mm)	(–)	(GPa)
550	600	17.5	30	0.85	500

First, the effect of the maximum normal traction of the GB is studied. For simplicity, a bilinear TSL ( $f_{G,I,II} = 0$ ) is used first. Moreover, in the first instance, the effects of the dissipated energy and shape of the TSL are disregarded: the fracture criterion is assumed to depend exclusively on mode I traction, tangential or mode II is assumed damageless:  $t_{2,I} \gg t_{1,II}$  in Eq. (13). The first

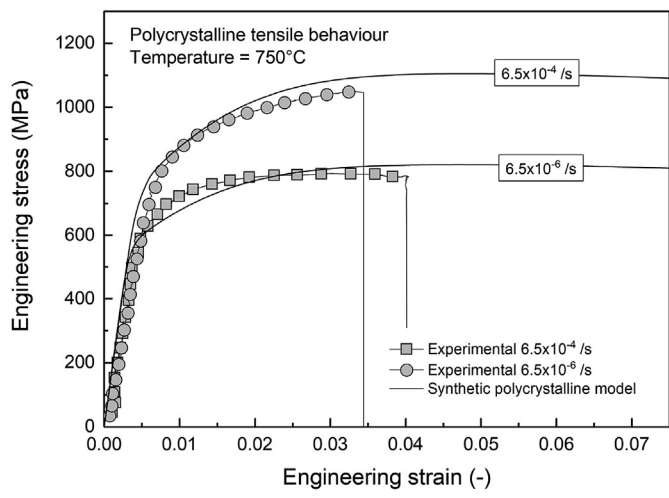


Fig. 12. Experimental polycrystalline tensile results versus model predictions for a synthetic microstructure without cohesive elements or damage at the grain boundaries.

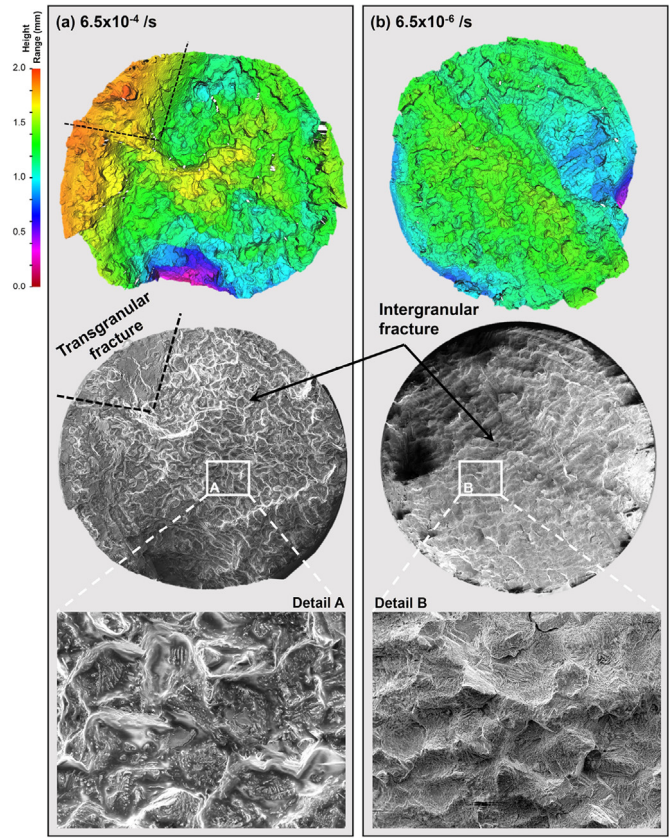
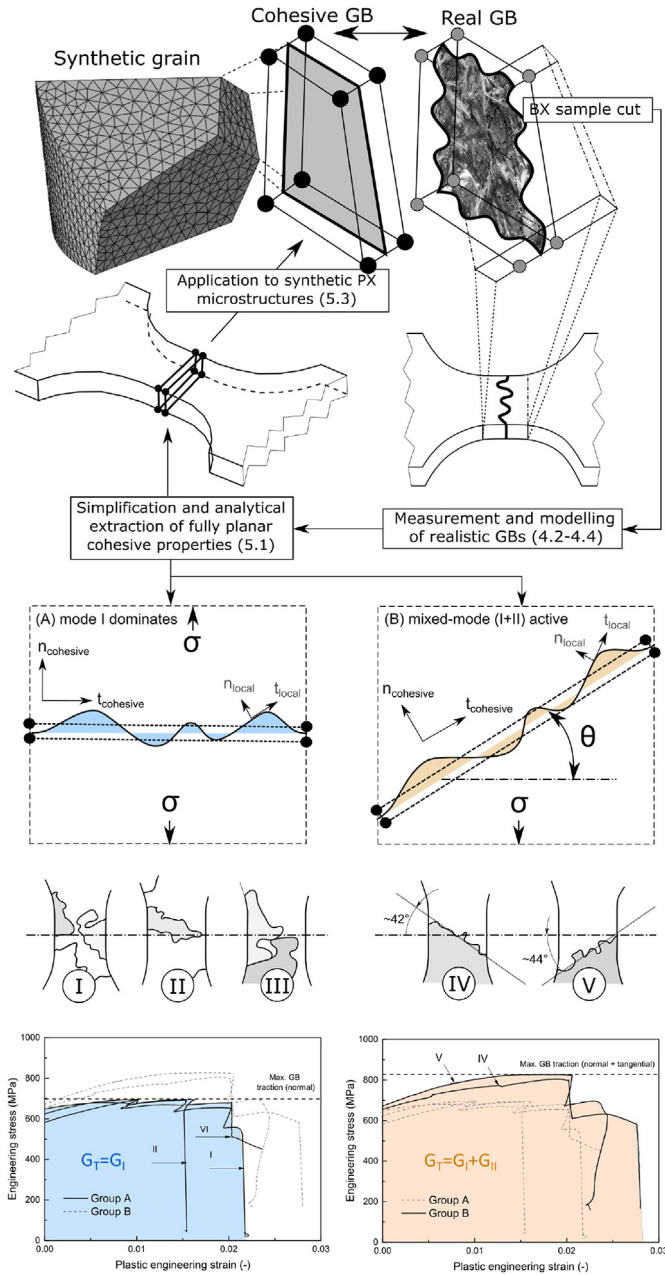


Fig. 13. Optical micrographs and surface measurements for each of the tested conditions: (a)  $6.5 \times 10^{-4}$ /s and (b)  $6.5 \times 10^{-6}$ /s.

column in Fig. 9 shows the model results for each one of the three samples presented previously for different values of the maximum normal traction  $t_{1,I} = 250, 500$ , and  $750$  MPa. One immediately observes that, without GB damage, the mechanical response of the samples is predicted to be significantly higher than that observed experimentally. This proves that the overall yielding behaviour of the samples is dominated by the cohesive strength of the grain boundary itself – the maximum experimental tensile strength is





**Fig. 14.** Process simplification to derive cohesive properties suitable for implementation in planar cohesive boundaries as generated in synthetic polycrystalline microstructures.

approximately 200–300 MPa lower than that predicted for perfectly joined grains. The maximum normal strength of the interface is approximately 500 MPa.

The second column of Fig. 9 shows the obtained stress-strain curves when introducing mode II failure – it shows that the maximum macroscopic strength is not controlled or affected greatly by the shear strength of the grain boundary. Its effect is noticeable after some of the normal grain boundaries have damaged. This highlights the importance of grain boundary engineering: large sections of planar grain boundaries are likely to influence negatively the cohesive strength of the interface.

In the third column, the shape and maximum strength of the cohesive boundary is considered. First, it is evident that a bilinear TSL is unsuitable to represent the GB behaviour. In order to capture

**Table 7**

Cohesive zone boundary model for quadratic damage initiation.

Group B	$\sigma$ (MPa)	$\theta$ (°)	$t_I$ (MPa)	$t_{II}$ (MPa)	$t_{I,I}$ (MPa)	$t_{I,II}$ (MPa)
Sample IV	805	41	607	528	700	1063
Sample V	826	43	604	563	700	1115

the behaviour accurately, a plateau – where the GB can deform without loss of strength – is necessary. Fig. 10 shows how the combination of the maximum traction in mode I and II affects the ultimate tensile strength of each specimen. From this, one may deduce that the maximum strength for the normal direction  $t_I$  is close to 550 MPa while the maximum tangential strength  $t_{II}$  is  $\approx 600$ –700 MPa.

In the fourth and last column, the energy release rate is calibrated – its value directly influences the amplitude of the TSL plateau which determines the strain to failure of the interface. The

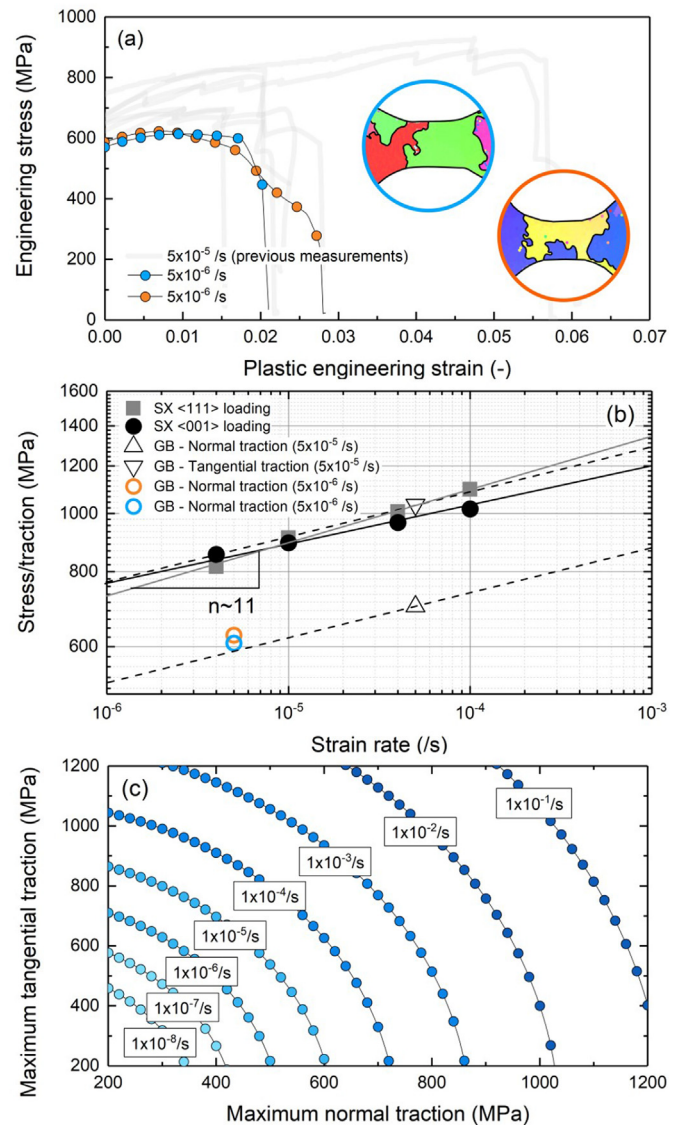


**Fig. 15.** (a) Bicrystalline experimental results at  $5 \times 10^{-6}$  s. (b) Rate dependent behaviour of the single-crystal alloy and the cohesive grain boundaries. (c) Maximum traction values for the proposed TSL as a function of the mode mixity and the rate of displacement.



consequences of different values of dissipated energy on the ductility is measured directly and illustrated in Fig. 11. It is found that a critical energy release rate between 15 and 20 N/mm reproduces accurately the measured behaviour. This is consistent with reasonable estimates of energy release rate in Ni-superalloys: employing the expression for the strain energy release rate  $G$

$$G = K_I^2 \left( \frac{1 - \nu^2}{E} \right) \quad (24)$$

where  $K_I$  is the stress intensity factor for mode I ( $\approx 60 \text{ MPa}\sqrt{\text{m}}$  for Ni-superalloys),  $\nu$  is the Poisson's ratio, and  $E$  is the elastic modulus ( $\approx 220 \text{ GPa}$ ), one obtains a energy release rate of  $\approx 18 \text{ N/mm}$ . The derived cohesive properties of the grain boundaries are summarised in Table 6. The results show that the explicit micro-models are able to rationalise the change in ductility as a function of the microstructure and specifically the grain boundary architecture. One should note that the cohesive properties derived here are rate independent, thus only valid for a particular strain-rate of interest – all the bicrystalline samples were tested at the same displacement rate. Nevertheless, in Section 5, the effect of rate on cohesion is introduced by comparing to further experiments in both bicrystalline and polycrystalline samples.

There is nonetheless a deviation between the modelled macroscopic behaviour and the one measured experimentally, and this is worthy of further more detailed consideration. Sources of error may include: (i) loss in strength due to intragranular damage which is not considered in the crystal plasticity model, and (ii) geometrical differences as the grain boundary extrudes towards the inside of the experimental samples – models assume that the same geometry is maintained through the thickness, and although the thickness is small when compared to the width of the sample, some differences may be present. Future work should address these points.

## 5. Further validation and application: polycrystalline microstructures

In this section, the reported findings are introduced into polycrystalline models. First, the single-crystal plasticity model is validated by comparing experimental tensile tests to simulations in a synthetic polycrystalline microstructure assuming grains which are perfectly joined. Second, fractography is used to elucidate the mechanisms of fracture in the experiments. Third, the derived traction separation laws are adapted to better represent the behaviour of grain boundaries as modelled in synthetic microstructures. Finally, the numerical representation of the grain structure is embedded with cohesive elements to capture damage – these simulations are used to validate the grain boundary cohesive zone model (which determines the strain-to-failure).

### 5.1. Model validation via polycrystalline tensile testing

In order to validate the models, constant displacement tensile tests in polycrystalline samples were performed. Two tensile samples were tested at a temperature of  $750^\circ\text{C}$  and strain rates of

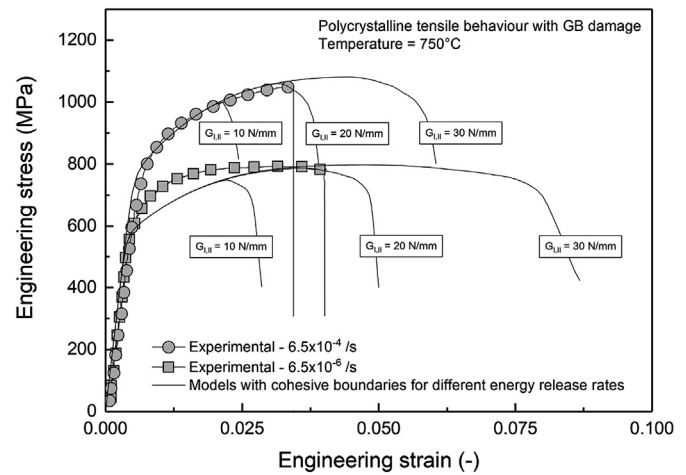


Fig. 16. Experimental polycrystalline tensile results versus model predictions for different values of dissipated energy.

$6.5 \times 10^{-4}$  and  $6.5 \times 10^{-6}/\text{s}$ . The results are shown as scattered points in Fig. 12. In this figure, the polycrystalline model predictions are compared to the experiments – the lines show the predictions from the polycrystalline model with perfectly joined grains – thus no damage is considered at the grain boundaries. One can see that the stress-strain response is accurately predicted – thus the proposed single crystal plasticity model can be considered physically faithful. However, the model is unable to predict ductility: it is necessary to introduce a mechanism of damage. To confirm whether failure was caused by grain boundaries, fractography was carried out. Fig. 13 shows the post-mortem surface of each experiment: the top of the figure shows the depth profile as measured in an Alicona profilometer, bottom side shows SEM micrographs of the whole fracture surface together with high-resolution details. From these, it is observed that the fracture is mainly intergranular – at a strain rate of  $6.5 \times 10^{-6}/\text{s}$  (b) the full surface represents intergranular failure while at  $6.5 \times 10^{-4}/\text{s}$  (a) only a very small part of the fracture surface is transgranular (area indicated in top of Fig. 13). It is therefore necessary to introduce the previously measured grain boundary properties into these models if one wants to include physically-based damage criteria.

### 5.2. Adapting the cohesive law to synthetic polycrystalline models

In the previous section, it has been shown that the grain boundary architecture and local orientation plays an important role on the strength and ductility of the alloy. However, when one uses Voronoi tessellation to produce synthetic microstructures, the grain boundaries are perfectly planar faces – the actual geometry of the boundary is not explicitly modelled (see top of Fig. 14). Thus, there is a need to simplify and adapt the manner in which we extract the GB properties from the experiments. To do so, the experimental results of miniaturised sections are necessary. One may assume that a single planar interface across the sample accounts for the strength and ductility of the whole boundary as illustrated in Fig. 14. This interface will store statistically all the factors which affect the strength of the boundary – e.g. serrations, segregation, misorientation. Thus, all one needs to do is to project the stresses on this virtual interface so that the maximum normal and tangential tractions can be quantified – see procedure described in Fig. 14. The first group of samples – those with the GBs oriented almost perpendicular to the loading axis – are used to determine the normal traction  $t_{1,1}$ . This is estimated to be

Table 8

Grain boundary properties parameters for cohesive elements when assuming planar faces and rate-dependency.

$t_{0,I}$	$t_{0,II}$	$\dot{\epsilon}_0$	$n_c$	$G_I^C$	$G_{II}^C$	$f_{G,I,II}$	$K_{I,II}$
(MPa)	(MPa)	(1/s)	(–)	(N/mm)	(N/mm)	(–)	(GPa)
1461	2159	1	13.4	20	20	0.9	500

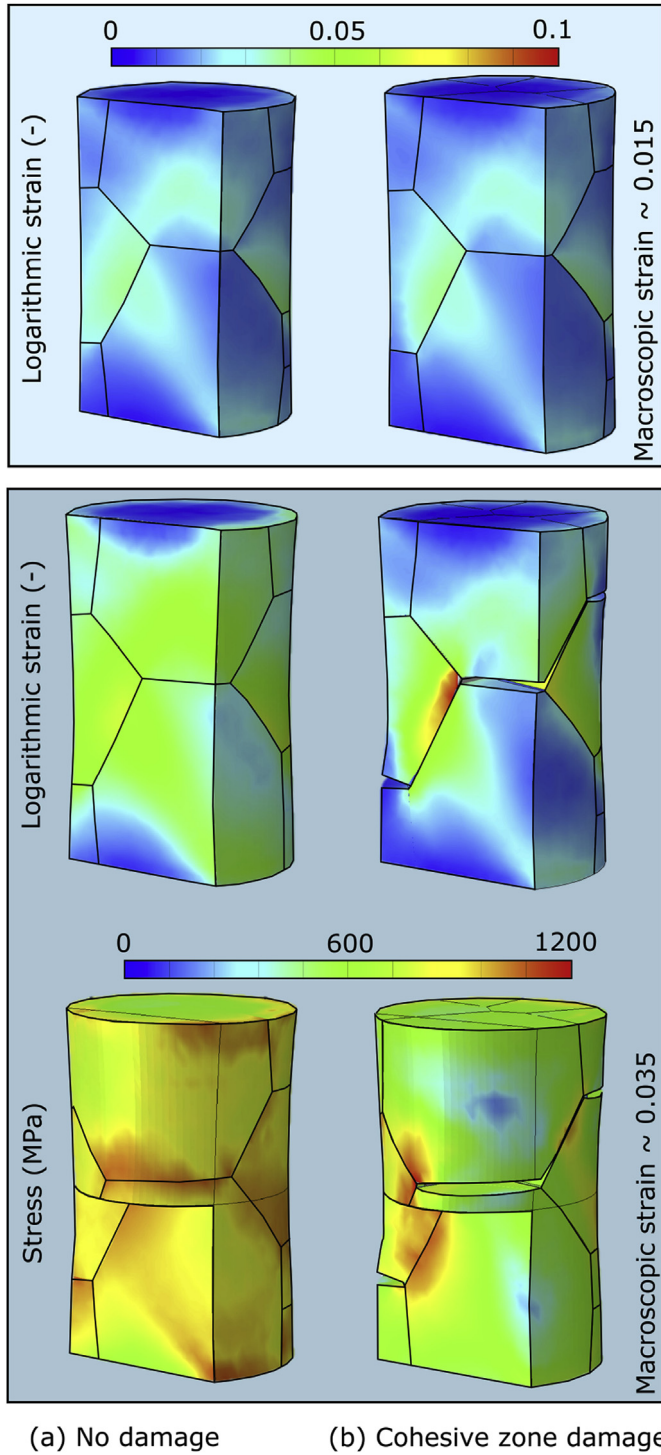


**Fig. 17.** Strain and stress distributions at different points during the test for models without and with damage at the grain boundaries when deformed at a strain rate of  $6.5 \times 10^{-6}/s$ .

approximately 700 MPa. With the normal behaviour determined, samples with angled grain boundaries can be used to derive the maximum tangential strength following  $t_I = \sigma \cos(\theta)$  and  $t_{II} = \sigma \sin(\theta)$ , where  $\theta$  is the angle of the interface with respect the loading axis. The derived normal and tangential maximum traction values when assuming a quadratic damage initiation criteria are summarised in Table 7.

Moreover, one may include the effect of the rate of deformation on the behaviour of the grain boundary. To measure the deformation rate effect, two more bicrystalline experiments were carried out at a strain rate of  $5 \times 10^{-6}/s$  – see Fig. 15(a). Results show a lower maximum stress than those measured previous but similar values of strain to failure. These are used to introduce the dependency of the rate on the maximum traction of the cohesive boundary as illustrated in Fig. 15(b). To include this into the cohesive zone model, a few changes to the previously proposed formulation are necessary. Now, it is assumed that the maximum tractions are a function of an equivalent grain boundary strain rate  $\dot{\epsilon}_{eq}$  following

$$\dot{\epsilon}_{eq} = \frac{\sqrt{\dot{\delta}_n^2 + \dot{\delta}_{t1}^2 + \dot{\delta}_{t2}^2}}{t_{element}} \quad (25)$$

where  $\dot{\delta}_n$  is the rate of separation in the normal direction of the cohesive element,  $\dot{\delta}_{t1}$  and  $\dot{\delta}_{t2}$  are the separation rates for each one of the tangential directions, and  $t_{element}$  is the thickness of the element – in this case zero thickness elements are used ( $t_{element} = 1$  mm). Then, the maximum tractions in mode I and II as used in Eq. (13) can be described following

$$t_{I,I} = t_{0,I} \left( \frac{\dot{\epsilon}_{eq}}{\dot{\epsilon}_0} \right)^{n_c} \quad (26)$$

$$t_{I,II} = t_{0,II} \left( \frac{\dot{\epsilon}_{eq}}{\dot{\epsilon}_0} \right)^{n_c} \quad (27)$$

where  $t_{0,I}$  and  $t_{0,II}$  are the reference values for the maximum traction in mode I and II respectively,  $\dot{\epsilon}_0$  is the reference strain rate value, and  $n_c$  is the maximum traction rate exponent. It should be noted that the equivalent strain rate is updated until the yield criterion ( $\delta_m \geq \delta_{1,m}$ ) is satisfied – after that, the traction value depends on the strain rate at yield initiation. The rate-dependent model was implemented using a UMAT user subroutine in Abaqus. The failure envelope obtained using the rate-dependent expressions on the quadratic initiation criteria expressed in Eq. (13) is shown in Fig. 15(c) for different values of equivalent strain rates. Table 8 shows the calibrated cohesive zone model parameters which are deduced.

### 5.3. On the influence of the grain boundary properties on the ductility

As a test of the above, Fig. 16 compares the tensile experiments with the polycrystalline models embedded with cohesive elements at the boundaries. The line-symbol curves show the stress-strain response for different values of critical energy release rates and the points illustrate the experimental points. The model with damage is able to accurately predict both the drop in strength due to the initiation of damage and the failure strain which occurs when the structural stability is lost. This confirms that: (i) the proposed crystal plasticity model is representative of the underlying high-temperature physics, and (ii) the drop in properties induced by decohesion is necessary to accurately predict the full behaviour.

Fig. 17 shows the accumulation of strain at different points during deformation for both models with and without grain boundary damage. Before damage initiates, both models predict the same distribution of strain. However, once damage initiates, the model with grain boundary decohesion shows a stronger inhomogeneity of strains – triple points where cracks are halted are indeed areas of high strain accumulation. The bottom side of Fig. 17 shows the von Mises stress distribution moments before final

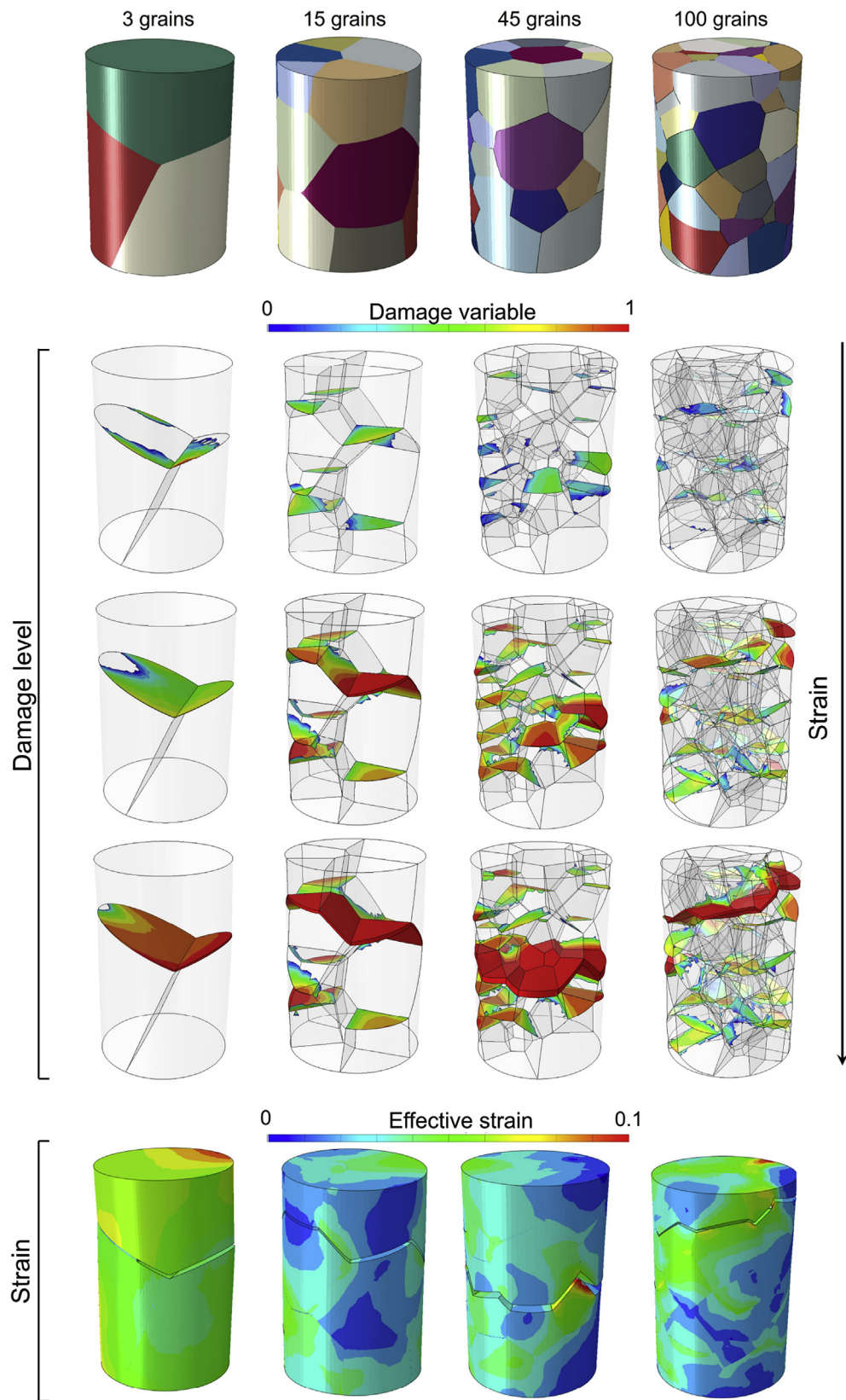
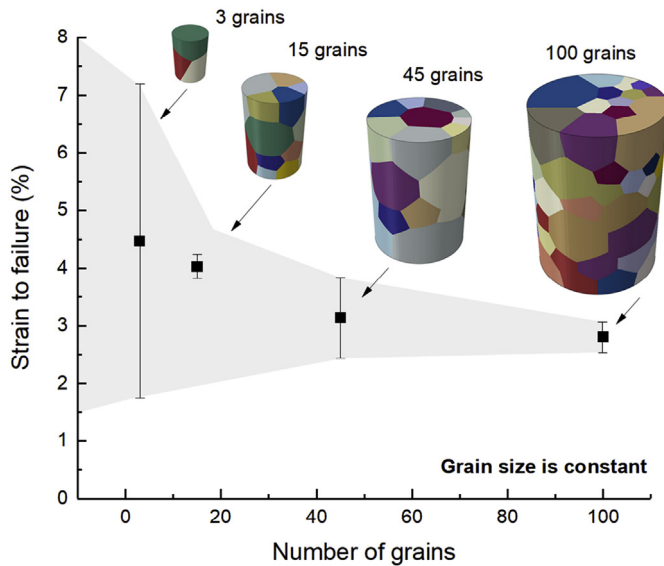


Fig. 18. Distribution of damage along the grain boundaries at different strain points for samples with different RVEs.





**Fig. 19.** Statistical representation of the strain-to-failure of synthetic samples with different number of grains and distributions when deformed at a strain rate of  $6.5 \times 10^{-6}$ /s.

fracture happens. Similar observations arise: stresses are relieved locally as the crack progresses while points still in cohesion suffer a higher stress load. As the rate of deformation increases, this stress concentration becomes higher and may cause the crack to propagate transgranularly as seen in Fig. 13(a). This indeed supports the hypothesis of a shift of the mechanics of damage – from intergranular to transgranular – between creep-like rates of deformation and medium-to-high deformation rates.

#### 5.4. On the influence of a representative volume element on the ductility

Fig. 18 shows the damage process of the grain boundaries at different strain points for volumes with different number of grains – from 3 to 100. For convenience, the mean grain size is kept constant, thus the synthetic samples with higher number of grains are also higher in volume. As observed previously, the GBs positioned perpendicularly to the loading axis are the ones which get damaged first – independently of the number of grains present. After this, damage propagates among inclined GBs until a web of degraded grain boundaries is fully connected and the final failure occurs. In Fig. 18, one may notice that, as the number of grains increases, the number of angled grain boundaries and their relative angle with respect to the loading axis is reduced – the crack can find an easy way through the thickness by linking the most optimal (from the fracture perspective) GBs from different individual grains. In this regard, Fig. 19 shows the ductility obtained as a function of the number of grains – at least three different microstructures were produced for each case so that a statistical representation can be given. One can observe that: (i) the ductility tends to converge to a defined value as the number of grain increases, and (ii) the deviation is higher for those samples with fewer grains. This is believed to be caused by the statistical probability of finding a linked web of close-to-perpendicular grain boundaries to the loading axis. Fig. 19 shows that, when a volume of 50–100 grains is achieved, the scatter in ductility is minimum – thus, from the fracture mechanics point of view, this number can be assumed as the RVE of the material.

## 6. Summary and conclusions

The following conclusions can be drawn from this work:

1. A combined experimental/modelling approach at different length scales has been used to study, observe and quantify the deformation behaviour of a polycrystalline nickel-based superalloy, taking specifically into account the grain boundary properties.
2. This has involved the *in-situ* observation within the SEM of the deformation behaviour of miniaturised testpieces containing relatively few grain boundaries at 750 °C; the scatter in ductility is significant and where low, is consistent with microstructural observations which confirm poorly orientated grains and/or grain boundaries. It follows that the gauge volume of the test-piece is below that of a true representative volume element; it is this situation which has allowed the situation to be analysed in detail.
3. The behaviour of the grain boundaries has been modelled and properties estimated using single crystal plasticity and cohesive zone modelling techniques. The maximum tractions of the grain boundaries are estimated as 550 and 600 MPa in the normal (mode I) and tangential (mode II) directions respectively. The energy release rate is estimated to be 17.5 N/mm for the fracture mode I – which is shown to be the critical mode for grain boundary failure.
4. For such reduced volumes of material, the modelling and experimentation prove that the grain boundaries are critical; the damage occurring at the grain boundaries determines both the levels of strength and ductility of the alloy – thus confirming that the interface is the weakest link. The local architecture of the grain boundary is responsible for the drop in mechanical properties: interfaces perpendicular to the loading axis tend to fail prematurely at strengths well below the macroscopic yield stress.
5. Grain boundary serration increases both the strength and the ductility of the alloy. Its effect on damage initiation sites and retardation of damage evolution is clear in both experiments and models. Serrations induce an inhomogeneous distribution of strain – this was observed *in-situ* and corroborated by simulations. This transgranular accumulation of strain induced by partial grain boundary decohesion is responsible for a transition from intergranular to transgranular failure which is observed under certain scenarios – those where the highest ductilities are achieved.
6. Polycrystalline experimentation under tension have further validated the proposed modelling framework. Synthetic microstructures – with parameters calibrated from SX tests – are able to predict accurately the high-temperature strength of the polycrystalline alloy. By adding interfacial elements at the grain boundaries, the observed mechanisms of failure are captured – after simplification, grain boundary properties calibrated from bicrystalline tensile tests are able to predict the strain-to-failure of polycrystalline microstructures.
7. Tests on different synthetic polycrystalline structures highlight the importance of having a representative volume element. If one stays below this, significant scatter in ductility is observed and the local orientation of the few grain boundaries present dictate the strain-to-failure of the material.
8. The modelling framework developed has the potential to be developed further for the formulation of new life prediction criteria suitable for creep, plasticity and fatigue, to include effects such as local strength differences arising from microstructural heterogeneities, for which the presence of grain boundaries is expected to play the crucial role.

## Acknowledgements

The authors of this paper are grateful to Siemens Industrial Turbomachinery AB for providing the studied material. The mechanical tests presented in this work were supported by the EPSRC under grant number EP/J013501/1, by the multifunctional high performance alloys for extreme environments program.

## Appendix A. Supplementary data

Supplementary data related to this article can be found at <https://doi.org/10.1016/j.actamat.2018.03.059>.

## References

- [1] P. Kontis, H.A.M. Yusof, S. Pedrazzini, M. Danaie, K.L. Moore, P.A.J. Bagot, M.P. Moody, C.R.M. Grovenor, R.C. Reed, On the effect of boron on grain boundary character in a new polycrystalline superalloy, *Acta Mater.* 103 (2016) 688–699.
- [2] A.A.N. Nemeth, D.J. Crudden, D.E.J. Armstrong, D.M. Collins, K. Li, A.J. Wilkinson, C.R.M. Grovenor, R.C. Reed, Environmentally-assisted grain boundary attack as a mechanism of embrittlement in a nickel-based superalloy, *Acta Mater.* 126 (2017) 361–371.
- [3] J.C. Stinville, N. Vanderesse, F. Bridier, P. Bocher, T.M. Pollock, High resolution mapping of strain localization near twin boundaries in a nickel-based superalloy, *Acta Mater.* 98 (2015) 29–42.
- [4] Y. Wang, D. Wang, G. Zhang, L. Lou, J. Zhang, Characterization of tilt and twist low angle grain boundaries and their effects on intermediate-temperature creep deformation behaviour, in: *Superalloys 2016: Proceedings of the 13th International Symposium on Superalloys*, 2016, pp. 757–762.
- [5] S.R. Yeratapally, M.G. Glavicic, M. Hardy, M.D. Sangid, Microstructure based fatigue life prediction framework for polycrystalline nickel-base superalloys with emphasis on the role played by twin boundaries in crack initiation, *Acta Mater.* 107 (2016) 152–167.
- [6] B. Larrouy, P. Villechaise, J. Cormier, O. Berteaux, Grain boundary slip bands interactions: impact on the fatigue crack initiation in a polycrystalline forged Ni-based superalloy, *Acta Mater.* 99 (2015) 325–336.
- [7] W.D. Musinski, D.L. McDowell, Simulating the effect of grain boundaries on microstructurally small fatigue crack growth from a focused ion beam notch through a three-dimensional array of grains, *Acta Mater.* 112 (2016) 20–39.
- [8] V. Randle, Twinning-related grain boundary engineering, *Acta Mater.* 52 (2004) 4067–4081.
- [9] T. Watanabe, S. Tsurekawa, Toughening of brittle materials by grain boundary engineering, *Mater. Sci. Eng.* 387–389 (2004) 447–455.
- [10] H.U. Hong, H.W. Jeong, I.S. Kim, B.G. Choi, Y.S. Yoo, C.Y. Jo, Significant decrease in interfacial energy of grain boundary through serrated grain boundary transition, *Phil. Mag.* 92 (2012) 2809–2825.
- [11] A. Wisniewski, J. Beddoes, Influence of grain-boundary morphology on creep of a wrought Ni-base superalloy, *Mater. Sci. Eng.* 510–511 (2009) 266–272.
- [12] H.U. Hong, I.S. Kim, B.G. Choi, M.Y. Kim, C.Y. Jo, The effect of grain boundary serration on creep resistance in a wrought nickel-based superalloy, *Mater. Sci. Eng.* 517 (2009) 125–131.
- [13] H. Danflou, M. Macia, T. Sanders, T. Khan, Mechanisms of formation of serrated grain boundaries in nickel base superalloys, in: *Superalloys 1996*, vol. 5, 1996, pp. 119–127, <https://doi.org/10.1023/A:1018694716756> [http://www.tms.org/superalloys/10.7449/1996/Superalloys\(1996\)119\(1\)127.pdf](http://www.tms.org/superalloys/10.7449/1996/Superalloys(1996)119(1)127.pdf).
- [14] R. Jiang, N. Gao, P.A.S. Reed, Influence of orientation-dependent grain boundary oxidation on fatigue cracking behaviour in an advanced Ni-based superalloy, *J. Mater. Sci.* 50 (2015) 4379–4386.
- [15] J.M. Larson, S. Floreen, Metallurgical factors affecting the crack growth resistance of a superalloy, *Metall. Trans. A* 8 (1977) 51–55.
- [16] T. Watanabe, An approach to grain-boundary design for strong and ductile polycrystals, *Res. Mech.* 11 (1984) 47–84.
- [17] T.P. Halford, K. Takashima, Y. Higo, P. Bowen, Fracture tests of micro-sized TiAl specimens, *Fatig. Fract. Eng. Mater. Struct.* 28 (2005) 695–701.
- [18] D.E.J. Armstrong, M.E. Rogers, S.G. Roberts, Micromechanical testing of stress corrosion cracking of individual grain boundaries, *Scripta Mater.* 61 (2009) 741–743.
- [19] D. Armstrong, A. Wilkinson, S. Roberts, Micro-mechanical measurements of fracture toughness of bismuth embrittled copper grain boundaries, *Phil. Mag. Lett.* 91 (2011) 394–400.
- [20] Y. Su, C. Zambaldi, D. Mercier, P. Eisenlohr, T. Bieler, M. Crimp, Quantifying deformation processes near grain boundaries in  $\beta_2$  titanium using nano-indentation and crystal plasticity modeling, *Int. J. Plast.* 86 (2016) 170–186.
- [21] S.R. Kalidindi, S.J. Vachhani, Mechanical characterization of grain boundaries using nanoindentation, *Curr. Opin. Solid State Mater. Sci.* 18 (2014) 196–204 (Slip Localization and Transfer in Deformation and Fatigue of Polycrystals).
- [22] D. Kupka, E.T. Lilleodden, Mechanical testing of solid-solid interfaces at the microscale, *Exp. Mech.* 52 (2012) 649–658.
- [23] F. Hofmann, E. Tarleton, R.J. Harder, N.W. Phillips, P.-W. Ma, J.N. Clark, I.K. Robinson, B. Abbey, W. Liu, C.E. Beck, 3D lattice distortions and defect structures in ion-implanted nano-crystals, *Sci. Rep.* 7 (2017) 45993.
- [24] J.A. El-Awady, C. Woodward, D.M. Dimiduk, N.M. Ghoniem, Effects of focused ion beam induced damage on the plasticity of micropillars, *Phys. Rev. B* 80 (2009) 104104.
- [25] W.D. Summers, E. Alabort, P. Kontis, F. Hofmann, R.C. Reed, In-situ high-temperature tensile testing of a polycrystalline nickel-based superalloy, *Mater. A. T. High. Temp.* 33 (2016) 338–345.
- [26] P. Kontis, E. Alabort, D. Barba, D.M. Collins, A.J. Wilkinson, R.C. Reed, On the role of boron on improving ductility in a new polycrystalline superalloy, *Acta Mater.* 124 (2017) 489–500.
- [27] T.R. Bieler, P. Eisenlohr, F. Roters, D. Kumar, D.E. Mason, M.A. Crimp, D. Raabe, The role of heterogeneous deformation on damage nucleation at grain boundaries in single phase metals, *Int. J. Plast.* 25 (2009) 1655–1683.
- [28] D. Kumar, T.R. Bieler, P. Eisenlohr, D.E. Mason, M.A. Crimp, F. Roters, D. Raabe, On predicting nucleation of microcracks due to slip-twin interactions at grain boundaries in duplex near  $\gamma$ -TiAl, *J. Eng. Mater. Technol.* 130 (2008) 021012.
- [29] A. Cruzado, J. Llorca, J. Segurado, Modeling cyclic deformation of inconel 718 superalloy by means of crystal plasticity and computational homogenization, *Int. J. Solid Struct.* 122 (2017) 148–161.
- [30] F. Roters, P. Eisenlohr, L. Hantcherli, D. Tjahjanto, T. Bieler, D. Raabe, Overview of constitutive laws, kinematics, homogenization and multiscale methods in crystal plasticity finite-element modeling: theory, experiments, applications, *Acta Mater.* 58 (2010) 1152–1211.
- [31] A. Cruzado, B. Gan, M. Jiménez, D. Barba, K. Ostolaza, A. Linaza, J.M. Molina-Aldareguia, J. Llorca, J. Segurado, Multiscale modeling of the mechanical behavior of IN718 superalloy based on micropillar compression and computational homogenization, *Acta Mater.* 98 (2015) 242–253.
- [32] A. Needleman, A continuum model for void nucleation by inclusion debonding, *J. Appl. Mech.* 54 (1987) 525.
- [33] X.P. Xu, A. Needleman, Numerical simulations of fast crack growth in brittle solids, *J. Mech. Phys. Solid.* 42 (1994) 1397–1434.
- [34] J.J.M. Arata, K.S. Kumar, W.A. Curtin, A. Needleman, Crack growth across colony boundaries in binary lamellar TiAl, *Mater. Sci. Eng.* 329–331 (2002) 532–537.
- [35] S. Hao, W.K. Liu, B. Moran, F. Vernerey, G.B. Olson, Multi-scale constitutive model and computational framework for the design of ultra-high strength, high toughness steels, *Comput. Meth. Appl. Mech. Eng.* 193 (2004) 1865–1908.
- [36] J.D. Clayton, D.L. McDowell, Homogenized finite elastoplasticity and damage: theory and computations, *Mech. Mater.* 36 (2004) 799–824.
- [37] J.D. Clayton, *Dynamic Plasticity and Fracture in High Density Polycrystals: Constitutive Modeling and Numerical Simulation*, vol. 53, 2005, <https://doi.org/10.1016/j.jmps.2004.06.009>.
- [38] P. Kontis, H.A.M. Yusof, S. Pedrazzini, M. Danaie, K.L. Moore, P.A.J. Bagot, M.P. Moody, C.R.M. Grovenor, R.C. Reed, On the effect of boron on grain boundary character in a new polycrystalline superalloy, *Acta Mater.* 103 (2016) 688–699.
- [39] R. J. R. Inelastic constitutive relations for solids : theory and its application, *J. Mech. Phys. Solid.* 19 (1971) 433–455.
- [40] R.J. Asaro, Crystal plasticity, *J. Appl. Mech.* 50 (1983) 921–934.
- [41] A.M. Cuitino, M. Ortiz, Computational modelling of single crystals, *Model. Simulat. Mater. Sci. Eng.* 1 (1993) 225–263.
- [42] R.J. Asaro, Micromechanics of crystals and polycrystals, *Adv. Appl. Mech.* 23 (1983) 1–115.
- [43] D. Peirce, R.J. Asaro, A. Needleman, Material rate dependence and localized deformation in crystalline solids, *Acta Metall.* 31 (1983) 1951–1976.
- [44] S. Feih, Modelling cohesive laws in finite element simulations via an adapted contact procedure in ABAQUS, *Mater. Res.* 1463 (2004) 475102.
- [45] R.D.S.G. Campilho, M.F.S.F. de Moura, J.J.M.S. Domingues, Using a cohesive damage model to predict the tensile behaviour of CFRP single-strap repairs, *Int. J. Solid Struct.* 45 (2008) 1497–1512.
- [46] I. Simonovski, G. Machina, Grain Boundary Modeling Issues with Cohesive Elements : Application to Intergranular Stress Corrosion Cracking, 2012.
- [47] S. Eliasson, A. Lundberg, Investigation and Comparison of Cohesive Zone Models for Simulation of Crack Propagation, 2015, pp. 1–5.
- [48] I. Scheider, Cohesive model for crack propagation analyses of structures with elastic plastic material behavior, GKSS research center, Geesthacht (2001) 1–41.
- [49] R. Quey, P.R. Dawson, F. Barbe, Large-scale 3D random polycrystals for the finite element method: generation, meshing and remeshing, *Comput. Meth. Appl. Mech. Eng.* 200 (2011) 1729–1745.
- [50] K. Carlsson, <https://github.com/KristofferC/Phon>, 2017.
- [51] D. Nouailhas, G. Cailletaud, Tension-torsion behavior of single-crystal superalloys: experiment and finite element analysis, *J. Plast.* 11 (1995) 451–470.
- [52] D. Bettge, W. Österle, “Cube slip” in near-[111] oriented specimens of a single-crystal nickel-base superalloy, *Scripta Mater.* 40 (1999).
- [53] T. Tinga, W.A.M. Brekelmans, M.G.D. Geers, Cube slip and non-Schmid effects in single crystal Ni-base superalloys, *Model. Simulat. Mater. Sci. Eng.* 18 (2010) 015005.